iScience

CellPress
OPEN ACCESS

Article

Betacellulin promotes tumor development and EGFR mutant lung cancer growth by stimulating the EGFR pathway and suppressing apoptosis

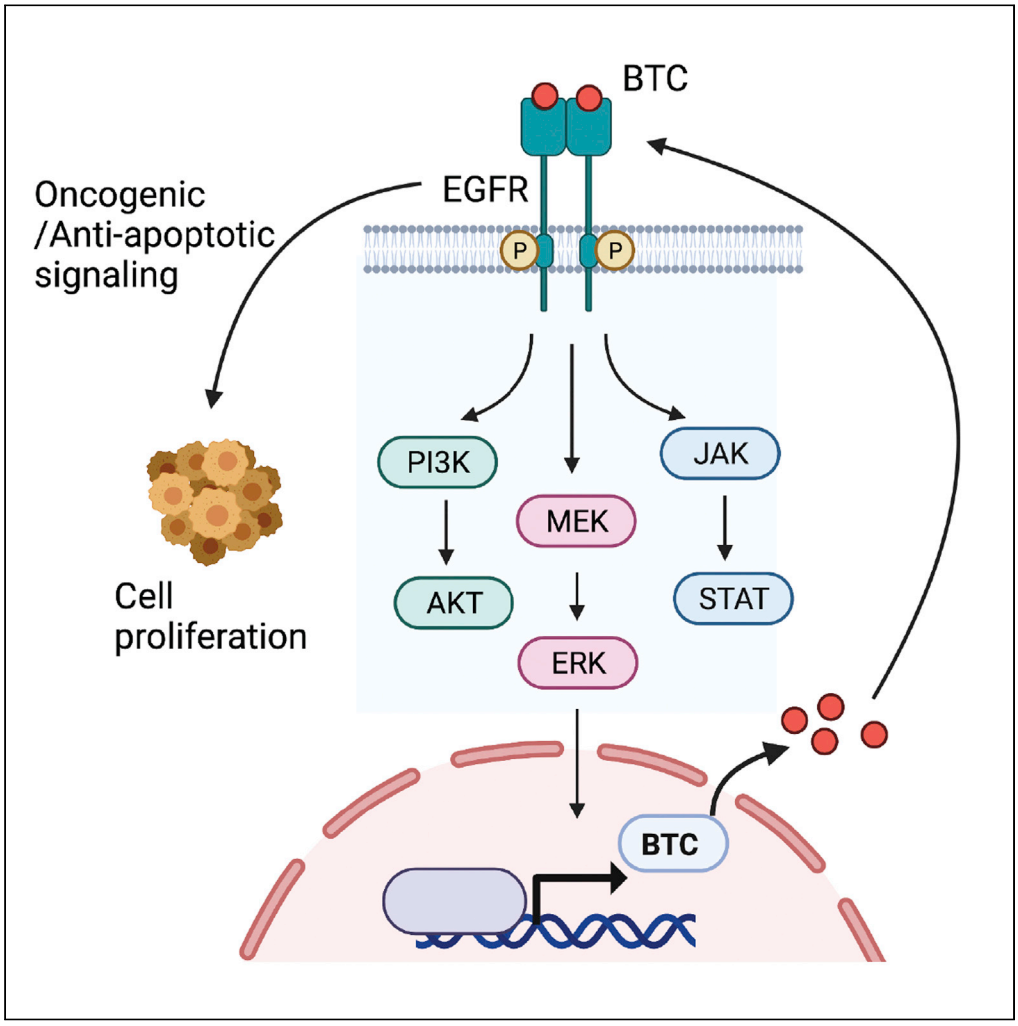

Suresh Chava,
Suresh Bugide,
Xuchen Zhang,
Romi Gupta,
Narendra
Wajapeyee

romigup@uab.edu (R.G.)
nwajapey@uab.edu (N.W.)

Highlights

BTC is a transcriptional target of oncogenic EGFR

BTC is overexpressed in patient-derived lung adenocarcinoma samples

BTC is necessary for EGFR-mutant lung adenocarcinoma tumor growth

Loss of BTC attenuates EGFR signaling and induces apoptosis

Chava et al., iScience *25*, 104211
May 20, 2022
https://doi.org/10.1016/j.isci.2022.104211

iScience

CellPress
OPEN ACCESS

Article

Betacellulin promotes tumor development and EGFR mutant lung cancer growth by stimulating the EGFR pathway and suppressing apoptosis

Suresh Chava,[1] Suresh Bugide,[1] Xuchen Zhang,[2] Romi Gupta,[1,3,*] and Narendra Wajapeyee[1,3,4,*]

SUMMARY

Oncogenic mutations in the *EGFR* gene account for 15–20% of lung adenocarcinoma (LUAD) cases. However, the mechanism for EGFR driven tumor development and growth is not fully understood. Here, using an mRNA expression profiling-based approach we identified betacellulin (*BTC*) as one the gene upregulated by oncogenic EGFR in an MAP kinase-dependent manner. BTC protein expression was markedly increased in LUAD patient samples compared to normal lung tissue, with higher expression in EGFR-mutant LUAD. *BTC* was sufficient to transform immortalized mouse cells, initiate tumor development in mice, and promote the survival of immortalized human lung epithelial cells. Conversely, knockdown of *BTC* inhibited the growth of EGFR-mutant human LUAD cells in culture and their tumor-forming ability in mice. Mechanistically, *BTC* knockdown resulted in attenuated EGFR signaling and apoptosis induction. Collectively, these results demonstrate a key role of BTC in EGFR-mutant LUAD, with potential therapeutic implications in LUAD and other EGFR-mutant cancers.

INTRODUCTION

Lung cancer is the most frequently diagnosed cancer in both men and women, and contributes to about 12% of total cancer cases and over 18% of total cancer-related deaths worldwide (Bray et al., 2018). Lung adenocarcinoma (LUAD) is the most common subtype of non-small cell lung cancer (NSCLC) and accounts for approximately 40% of all diagnosed lung cancers (Dela Cruz et al., 2011; Rau et al., 2016).

Genome-scale studies have identified several actionable oncogenic mutations in LUAD that include mutations in the epidermal growth factor receptor gene (*EGFR*) and translocations in the anaplastic lymphoma kinase gene (*ALK*) and the protein tyrosine kinase oncogenes *RET* and *ROS* genes (Ding et al., 2008; Govindan et al., 2012). Somatic mutations in *EGFR*, which encodes a receptor tyrosine kinase (RTK), are most commonly observed in LUAD and predominantly occur in non-smokers and patients of Asian descent. *EGFR* is located on human chromosome seven and encodes a 170-kDa protein with tyrosine kinase activity. EGFR belongs to the HER/ERBB family of RTKs. The human HER/ERBB family of RTKs includes ERBB1 (EGFR, also known as HER1), ERBB2 (HER2), ERBB3 (HER3), and ERBB4 (HER4). It has been shown that homodimerization and/or heterodimerization with other family members in response to ligand binding most commonly with HER2, which lacks its own specific ligand, and activates the tyrosine kinase (Yarden and Sliwkowski, 2001). Mutations in or amplifications of *ERBB2*, *ERBB3*, and *ERBB4* have also been shown to occur in lung adenocarcinoma, albeit at a lower frequency than alterations in *EGFR* (Cancer Genome Atlas Research Network, 2014).

More than 10 different ligands that bind to the ERBB family of RTKs have been identified. Among these is betacellulin (BTC), which was first identified in the conditioned medium of a cell line derived from mouse beta cell tumors and acts as a potent mitogen for retinal pigment epithelial cells and vascular smooth muscle cells (Shing et al., 1993). BTC binds to EGFR, ERBB3, and ERBB4 and promotes heterodimerization among ERBB family members (Pinkas-Kramarski et al., 1998; Singh et al., 2016; Singh and Coffey, 2014). BTC plays a wide variety of roles in cancer, including causing resistance to STAT3 inhibitors in glioblastoma (Fan et al., 2020), promoting vascularity in hepatocellular carcinoma by activating EGFR in endothelial cells in a paracrine manner (Moon et al., 2006), and increasing ovarian cancer cell migration by upregulating the gap junction protein Connexin43 (Zhao et al., 2020).

[1]Department of Biochemistry and Molecular Genetics, University of Alabama at Birmingham, Birmingham, AL 35233, USA

[2]Department of Pathology, Yale University, New Haven, CT 06510, USA

[3]O'Neal Comprehensive Cancer Center, University of Alabama at Birmingham, Birmingham, AL 35233, USA

[4]Lead contact

*Correspondence: romigup@uab.edu (R.G.), nwajapey@uab.edu (N.W.)

https://doi.org/10.1016/j.isci.2022.104211

Here, we showed that lung cancer-associated EGFR mutations drive the expression of BTC in an EGFR→MEK→ERK signaling pathway-dependent manner. Furthermore, we showed that BTC is overexpressed in patient-derived LUAD samples, that ectopically expressed BTC is sufficient to cause cellular transformation, and that *BTC* expression was necessary for the growth of EGFR-mutant LUAD cells. We also showed that BTC is both necessary and sufficient to activate EGFR signaling, thereby suppressing apoptosis induction and thus establishing a role for BTC in EGFR-driven tumor growth.

RESULTS

Generation of an isogenic cell system to study the function of lung adenocarcinoma-associated oncogenic EGFR mutants

Mutations in *EGFR* are present in approximately15% of all non-small cell lung cancers, and 45 different *EGFR* mutations have been cataloged by TCGA. Many of these mutations affect the tyrosine kinase domain and result in constitutive activation of EGFR signaling (Figure 1A and Table S1). To identify the transcriptional targets and potential regulators of oncogenic EGFR signaling resulting from specific LUAD-associated EGFR mutations, we generated several modified NIH3T3 cell lines that expressed an empty vector control, a wild-type EGFR control, or one of three commonly occurring LUAD-associated EGFR mutations: EGFR-L858R, EGFR-L861Q, or EGFR-DEL1. Compared to cells containing the empty vector or expressing wild-type EGFR, all three mutants showed potentiated EGFR signaling, as observed by higher levels of phosphorylated EGFR (*p*-EGFR), phosphorylated ERK1/2 (*p*-ERK1/2), and phosphorylated AKT (*p*-AKT) in all three mutants and higher levels of phosphorylated STAT5 (p-STAT5) in two (EGFR-L858R and EGFR-L861Q) out of three mutants (EGFR-L858R and EGFR-L861Q and EGFR-DEL1) (Figure 1B). Consistent with the role of EGFR in activating the MAP kinase, PI3K/AKT, and JAK/STAT pathway, treatment with EGFR inhibitor erlotinib resulted in reduced *p*-ERK1/2, *p*-AKT, and/or p-STAT5 to various degrees in wild-type or mutant EGFR-expressing cells (Figure 1B). Similarly, treatment with EGFR-TKI (erlotinib) resulted in reduced *p*-ERK1/2, *p*-AKT, and/or p-STAT5 in human lung adenocarcinoma cells (PC9) (Figure S1).

In addition, mutant EGFR-transformed NIH3T3 cells, but not empty vector or wild-type EGFR controls, grew in an anchorage-independent manner (Figures 1C and 1D) and avoided detachment-induced cell death (anoikis induction) (Figure 1E). These EGFR-transformed NIH3T3 cells were also addicted to EGFR signaling because treatment with the EGFR tyrosine kinase inhibitor (TKI) erlotinib inhibited the growth of NIH3T3 cells expressing mutant EGFR compared to the empty vector and wild-type EGFR controls (Figure 1F). Collectively, these results suggest that this cell system can be used to identify genes that are critical for EGFR-induced cellular transformation, tumor growth, and response to EGFR TKI therapy.

BTC is upregulated in response to oncogenic EGFR activity both in mouse NIH3T3 cells and human lung adenocarcinoma cell lines

After characterizing the empty vector-, wild-type-, and mutant EGFR-expressing NIH3T3 cells, we subjected them to RNA-seq analysis (Figure 2A). Ingenuity pathway analysis of the RNA-seq data revealed that several pathways (e.g., axonal guidance signaling, kinetochore metaphase signaling) were commonly regulated in all three EGFR mutant-expressing cell lines (Figure S2 and Tables S2, S3, S4, S5, S6, and S7). We chose 13 genes that were in common among the top 20 most upregulated genes in all of the EGFR mutant cell lines, compared to the controls, for validation by RT-qPCR (Figure 2B and Table S8). We found that *Arhgap6*, *Btc*, *Evi2a*, Calr4, *Gpr149*, *Sema7a*, and *Sema6d* were significantly upregulated in NIH3T3 cells expressing either EGFR-L858R, EGFR-L861Q, or EGFR-DEL1, but not in cells expressing the empty vector or wild-type EGFR (Figure 2C). Arhgap6 is a Rho GTPase shown to play a role in cancer growth and progression (Li et al., 2020; Wu et al., 2019). Sema7a and Sema6d are secreted proteins belonging to the semaphorin family of proteins (Hu and Zhu, 2018). Sema6d has been shown to predict improved survival in triple-negative breast cancer (Chen et al., 2015). EVi2a is a poorly studied gene, which might function as a cell-surface receptor and has been shown to promote and predict poor prognosis in cancers, including osteosarcoma (Li et al., 2019). Calr4 is a calcium-binding protein with no documented role in cancer. Gpr149 is a G protein–coupled receptor, and the hypermethylation of the Gpr149 promoter has been shown to predict poor cancer outcomes (Kim et al., 2019). Because Sema7a was previously shown to be important for *EGFR*-mutant LUAD (Kinehara et al., 2018), we did not include this gene for further analysis.

To determine whether any of above-identified upregulated genes might be the direct targets of oncogenic EGFR signaling, we treated NIH3T3 cells expressing EGFR-DEL1 with increasing concentrations of erlotinib and asked whether it inhibited their expression (Figure 3A). We found that of the six tested genes (*Arhgap6*,

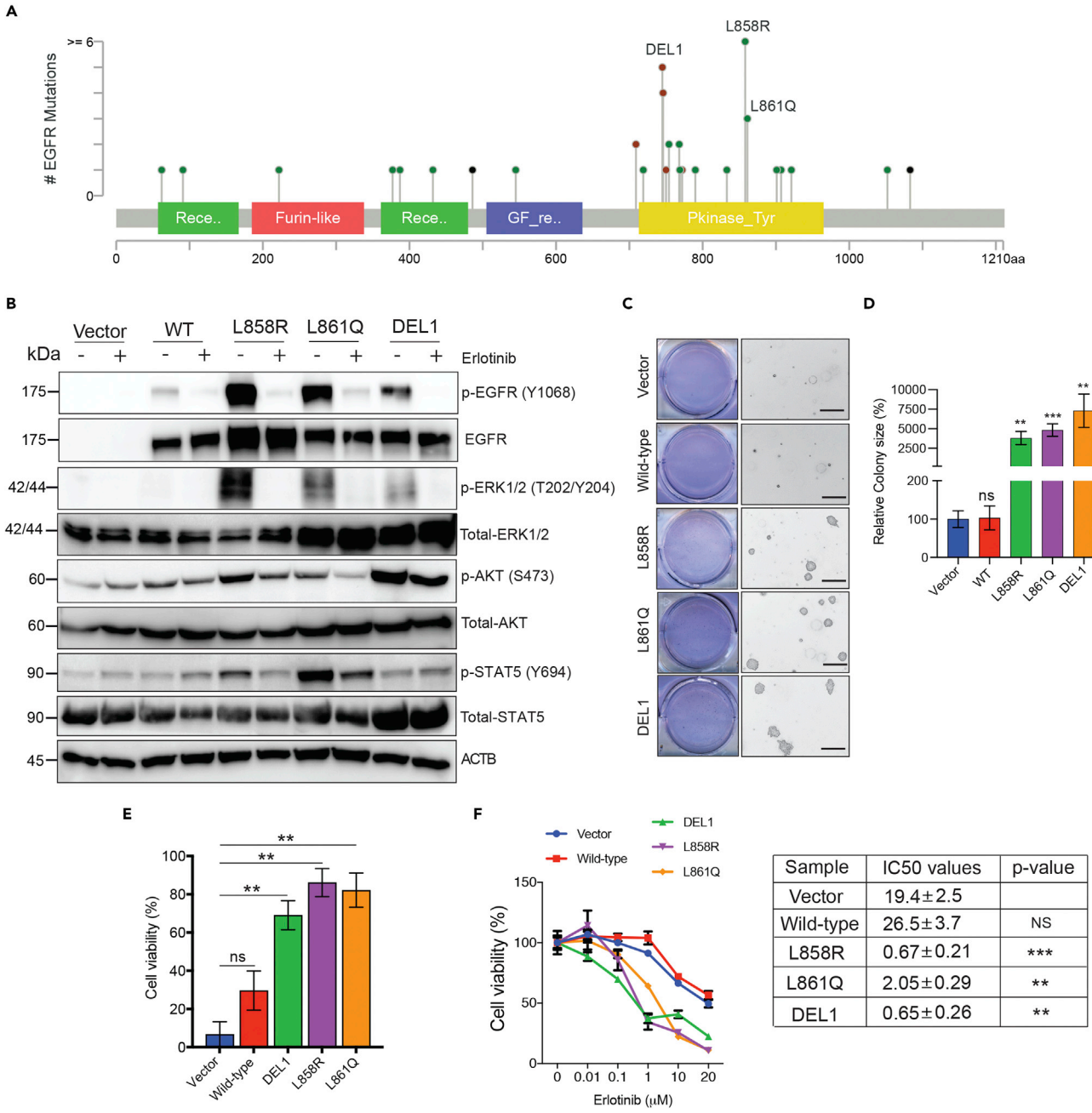

Sample	IC50 values	p-value
Vector	19.4±2.5	
Wild-type	26.5±3.7	NS
L858R	0.67±0.21	***
L861Q	2.05±0.29	**
DEL1	0.65±0.26	**

Figure 1. Lung adenocarcinoma-specific oncogenic EGFR mutations induce NIH3T3 transformation and cause sensitivity to an EGFR tyrosine kinase inhibitor

(A) Representative schematic showing the location of the lung adenocarcinoma (LUAD)-specific EGFR mutations [DEL1(E746-A750), L858R, and L861Q] used in this study.

(B) NIH3T3 cells expressing either empty vector, wild-type EGFR, or the indicated EGFR mutants were treated with erlotinib (1 μM) for 24 h and analyzed for the indicated proteins by immunoblotting. ACTB was used as a loading control.

(C) NIH3T3 cells expressing either empty vector, wild-type EGFR, or the indicated EGFR mutants were analyzed for anchorage-independent growth in a soft agar assay. Representative images of the wells and microscopic pictures are shown. Scale bar, 200 μm.

(D) Relative colony size (%) for the data shown in panel (C).

(E) NIH3T3 cells expressing empty vector, wild-type EGFR, or the indicated EGFR mutants were analyzed for survival under detached conditions using ultra-low attachment plates. The percentage of cells surviving after 3 days is shown.

(F) NIH3T3 cells expressing empty vector, wild-type EGFR, or the indicated EGFR mutants were analyzed for erlotinib (EGFR TKI) sensitivity in an MTT assay. The percentage of viable cells at 5 days after treatment with the indicated erlotinib concentrations are shown (left). IC_{50} values are shown on the right. Data are shown as the mean ± SEM, ns = not significant, **p<0.01, ***p<0.001. See also Figure S1 and Table S1.

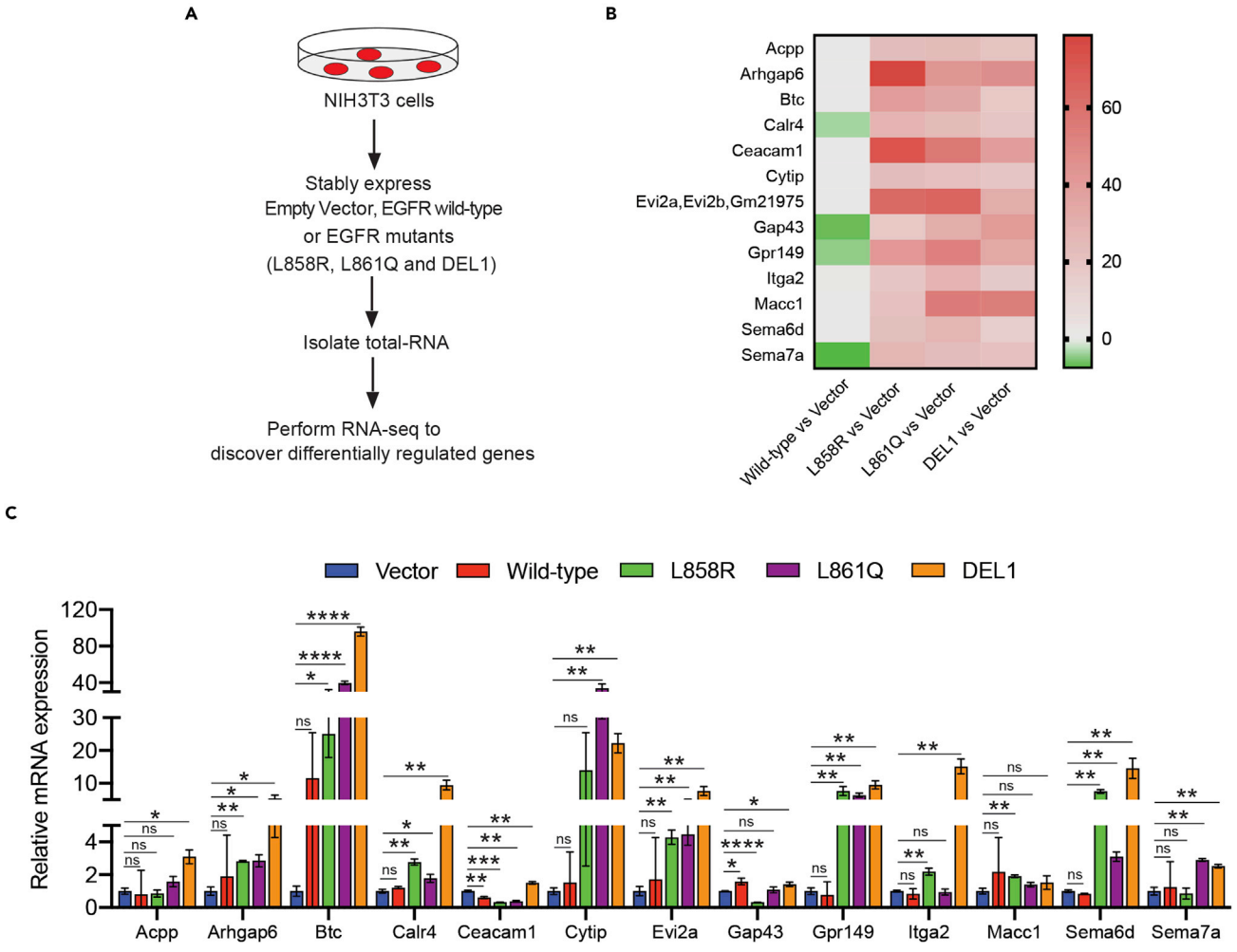

Figure 2. RNA-seq validation of the top upregulated genes in EGFR mutants

(A) Schematic showing the steps of RNA-seq for identifying commonly upregulated genes in NIH3T3 cells expressing the indicated EGFR mutants.

(B) RNA-seq was performed using NIH3T3 cells expressing either empty vector EGFR-WT or EGFR mutants L858R, L861Q, or DEL1. The heatmap showing the top upregulated genes whose expression was upregulated 15-fold or more in all mutants compared to the empty vector control.

(C) NIH3T3 cells expressing vector, wild-type EGFR or the indicated EGFR mutant were analyzed by RT-qPCR for expression of the indicated genes. Gene expression is plotted relative to the empty vector control. Data are shown as the mean ± SEM, ns = not-significant, *p<0.05, **p<0.01, ***p<0.001, ****p<0.0001. See also Figure S2 and Tables S2, S3, S4, S5, S6, S7, and S8.

Btc, *Evi2a*, *Calr4*, *Gpr149*, and *Sema6d*), only *Btc* expression showed significant and dose-dependent downregulation (Figure 3B). Next, we tested the expression of the same six genes (*ARHGAP6*, *BTC*, *EVI2A*, *CALR3*, *GPR149*, and *SEMA6D*) after treatment with erlotinib in PC9 human lung cancer cells, which bear a deletion in *EGFR* analogous to the NIH3T3-DEL1 mutant (Figure 3C). Similar to mouse NIH3T3-DEL1 cells, *BTC* expression was reduced after erlotinib treatment in human EGFR mutant PC9 cells (Figure 3D). In additional, expression of *ARHGAP6* and *GRP149* was also inhibited in the PC9 cells treated with erlotinib (Figure 3D). Furthermore, treatment of another EGFR mutant human lung cancer cell HCC2935 with erlotinib resulted in downregulation of *BTC* and *EVI2A* (Figure S3A). Based on the collective results from all three cell lines (NIH3T3-DEL1, PC9 and HCC2935) identified BTC as the common candidate that was regulated by EGFR signaling. To determine which signaling pathways downstream of EGFR might activate BTC expression, we treated NIH3T3-DEL1 cells and PC9 cells with the MEK inhibitor trametinib, the PI3K inhibitor pictilisib, and the JAK/STAT pathway inhibitor ruxolitinib. We found that treatment with trametinib, but not pictilisib or ruxolitinib, inhibited *BTC* expression (Figures 3E–3H and S3B–S3I) in these cells. To further establish the role of MAP kinase pathway in upregulation of BTC, we ectopically expressed a constitutively active form of MEK (MEK-DD) (Boehm et al., 2007) in NIH3T3 cells. Similar to our results with MEK inhibitors,

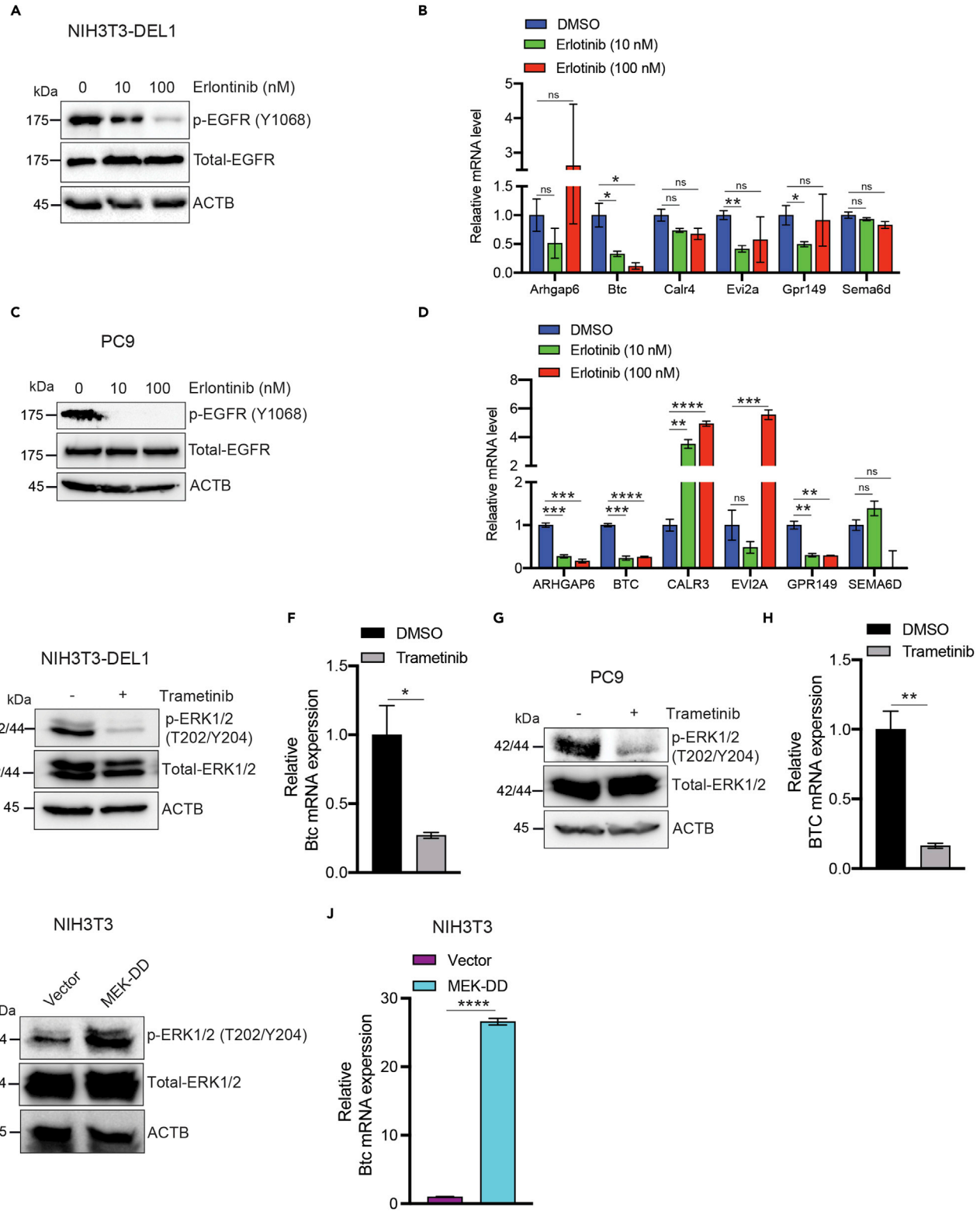
A
NIH3T3-DEL1
kDa
0
10
100
Erlontinib (nM)
175
p-EGFR (Y1068)
175
Total-EGFR
45
ACTB
B
DMSO
Erlotinib (10 nM)
Erlotinib (100 nM)
Relaative mRNA level
Arhgap6
Btc
Calr4
Evi2a
Gpr149
Sema6d
C
PC9
kDa
0
10
100
Erlontinib (nM)
175
p-EGFR (Y1068)
175
Total-EGFR
45
ACTB
D
DMSO
Erlotinib (10 nM)
Erlotinib (100 nM)
Relaative mRNA level
ARHGAP6
BTC
CALR3
EVI2A
GPR149
SEMA6D
E
NIH3T3-DEL1
kDa
-
+
Trametinib
42/44
p-ERK1/2 (T202/Y204)
42/44
Total-ERK1/2
45
ACTB
F
DMSO
Trametinib
Relative Btc mRNA expersion
G
PC9
kDa
-
+
Trametinib
42/44
p-ERK1/2 (T202/Y204)
42/44
Total-ERK1/2
45
ACTB
H
DMSO
Trametinib
Relative BTC mRNA expersion
I
NIH3T3
Vector
MEK-DD
kDa
42/44
p-ERK1/2 (T202/Y204)
42/44
Total-ERK1/2
45
ACTB
J
NIH3T3
Vector
MEK-DD
Relative Btc mRNA expersion

Figure 3. The EGFR→MEK→ERK kinase pathway is necessary for mutant EGFR-driven BTC expression

(A) NIH3T3-DEL1 cells were treated with either DMSO or 10 or 100 nM of erlotinib for 6 h. Indicated proteins were analyzed by immunoblotting. ACTB was used as a loading control.

(B) NIH3T3-DEL1cells were treated with DMSO or erlotinib (10 or 100 nM) for 6 h. Relative mRNA expression for the indicated genes was analyzed by RT-qPCR and plotted relative to that of DMSO-treated NIH3T3-DEL1 cells.

(C) PC9 cells were treated with DMSO or erlotinib (10 or 100 nM) for 6 h. Indicated proteins were analyzed by immunoblotting. ACTB was used as a loading control.

(D) PC9 cells were treated with DMSO or erlotinib (10 or 100 nM) for 6 h. Relative mRNA expression for the indicated genes was analyzed by RT-qPCR and plotted relative to that of DMSO treated PC9 cells.

(E) NIH3T3-DEL1 cells were treated with DMSO or trametinib (250 nM) for 24 h. Indicated proteins were analyzed by immunoblotting. ACTB was used as a loading control.

(F) NIH3T3-DEL1 cells were treated with DMSO or trametinib (250 nM) for 24 h. Relative *Btc* mRNA expression was analyzed by RT-qPCR and plotted relative to that of DMSO-treated NIH3T3-DEL1 cells.

(G) PC9 cells were treated with DMSO or trametinib (250 nM) for 24 h. Indicated proteins were analyzed by immunoblotting. ACTB was used as a loading control.

(H) PC9 cells were treated with DMSO or trametinib (250 nM) for 24 h. Relative *BTC* mRNA expression was analyzed by RT-qPCR and plotted relative to that of DMSO-treated PC9 cells.

(I) NIH3T3 cells expressing either empty vector or constitutively active MEK (MEK-DD) were analyzed for the indicated proteins. ACTB was used as a loading control.

(J) Relative *Btc* mRNA expression in NIH3T3 cells expressing either empty vector or MEK-DD were analyzed by RT-qPCR and plotted relative to empty vector-expressing NIH3T3 cells. Data are shown as the mean ± SEM, ns = not significant, *p<0.05, **p<0.01, ***p<0.001, ****p<0.0001. See also Figure S3.

we found that ectopic expression MEK-DD resulted in increased BTC expression (Figures 3I and 3J). These results demonstrate that EGFR activates the expression of *BTC* in an MAP kinase-dependent manner. Based on these collective results, we next focused our studies on BTC and its role in EGFR-induced LUAD tumor growth.

BTC is overexpressed in patient-derived samples of lung adenocarcinoma

Based on the results above, we investigated whether BTC protein expression is upregulated in LUAD cells using immunohistochemistry performed on LUAD tissue microarrays. The first array we examined (BS04081a, US Biomax) had 60 LUAD cores and three adjacent normal lung tissue cores. We found that BTC protein expression was significantly higher in LUAD samples compared with matched normal adjacent lung samples (Figures 4A, 4B, and Table S9). To further validate these findings, we analyzed a second tissue microarray (HLugA180Su03, US BioMax) with 89 patient-derived LUAD samples and 82 adjacent normal lung tissue samples. Similar to the first tissue array, there was a significant increase in BTC protein signal in tumors compared to normal adjacent lung tissues (Figures 4C, 4D, and Table S10). Finally, we asked whether the overexpression of BTC was restricted to LUAD tumors bearing mutations in EGFR by analyzing a microarray with 41 KRAS-mutant LUAD, 27 EGFR-mutant LUAD, and 57 KRAS/EGFR wild-type LUAD samples. We found that roughly the same percentage of all genomic subtypes of LUAD expressed BTC; however, the percentage of samples that showed strong (+3) BTC protein expression was somewhat higher in EGFR-mutant samples (37% for EGFR-mutant LUAD, 31% for KRAS-mutant LUAD, and 22% for EGFR/KRAS wild-type LUAD) (Figures 4E, 4F, and Table S11). Collectively, these results revealed that BTC is overexpressed in LUAD, and its expression is higher in EGFR-mutant LUADs than in KRAS-mutated or KRAS/EGFR wild-type LUADs.

BTC is sufficient to cause cellular transformation of NIH3T3 cells and promote anchorage-independent growth of immortalized human lung epithelial cells

Based on the results that BTC expression requires EGFR-MAPK-ERK signaling, we asked whether ectopic expression of *BTC* is sufficient to transform NIH3T3 cells. To this end, we introduced either an empty vector or *BTC* into NIH3T3 cells and asked first whether the cells could grow in an anchorage-independent manner in soft agar and next whether they could form tumors in mice. We found that ectopic expression of BTC resulted in significantly larger colonies in soft agar assays (Figures 5A and 5B), confirming that ectopic expression of *BTC* promotes anchorage-independent growth. Next, we subcutaneously injected NIH3T3 cells containing either an empty vector or a vector encoding *BTC* into immunocompromised mice. Consistent with our soft agar assays, all five mice injected with NIH3T3 cells expressing *BTC* formed tumors that grew over time. In contrast, of the five mice injected with NIH3T3 cells bearing the empty vector control, two failed to develop tumors, and three developed only very small tumors that did not progress (Figure 5C), which were likely because of spontaneous transformation of NIH3T3 cells. These results show that ectopic expression of *BTC* is sufficient for cellular transformation of NIH3T3 cells.

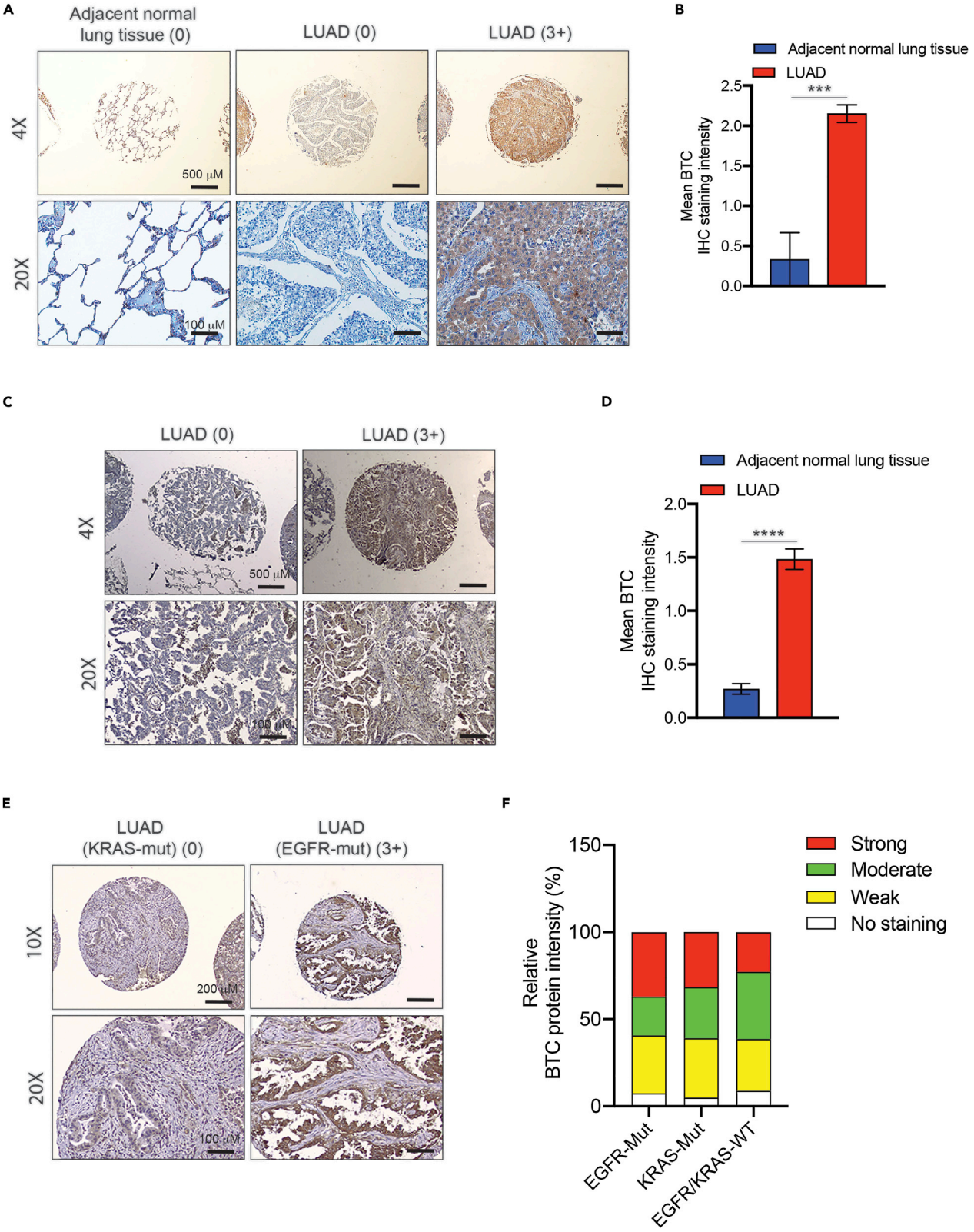
A
Adjacent normal lung tissue (0)
LUAD (0)
LUAD (3+)
4X
20X
500 μM
100 μM
B
Adjacent normal lung tissue
LUAD
***
Mean BTC IHC staining intensity
2.5
2.0
1.5
1.0
0.5
0.0
C
LUAD (0)
LUAD (3+)
4X
20X
500 μM
100 μM
D
Adjacent normal lung tissue
LUAD
****
Mean BTC IHC staining intensity
2.0
1.5
1.0
0.5
0.0
E
LUAD (KRAS-mut) (0)
LUAD (EGFR-mut) (3+)
10X
20X
200 μM
100 μM
F
Strong
Moderate
Weak
No staining
Relative BTC protein intensity (%)
150
100
50
0
EGFR-Mut
KRAS-Mut
EGFR/KRAS-WT

Figure 4. BTC is overexpressed in lung adenocarcinoma

(A) BTC expression was analyzed by immunohistochemistry (IHC) using a US BioMax tissue microarray (BS04081a), consisting of LUAD (60 cores) and normal lung tissues (3 cores). Representative normal lung and LUAD images at 4× and 20× magnifications are shown.

(B) Average BTC staining intensity in normal lung versus LUAD tissues (BS04081a) is plotted.

(C) BTC expression was analyzed by IHC using a US BioMax tissue microarray (HLugA180Su03) consisting of LUAD (n = 89) and normal adjacent lung tissues (n = 82). Representative LUAD images at 4× and 20× magnifications are shown.

(D) Average BTC staining intensity in normal lung versus LUAD (HLugA180Su03) is plotted.

(E) BTC expression was analyzed by IHC using the Yale University TMA (YTMA-310) consisting of LUAD tumors bearing mutations with KRAS-mutant(n = 41), EGFR-mutant(n = 27), and KRAS/EGFR wild-type(n = 57) LUAD samples. Representative LUAD images at 10× and 20× magnifications are shown.

(F) Relative BTC staining intensity in normal lung versus LUAD (YTMA310) is plotted. Data are shown as the mean ± SEM, ***p<0.001, ****p<0.0001. See also Tables S9, S10, and S11.

To test the impact of ectopic *BTC* expression in the context of human lung epithelial cells, we used human airway epithelial cells (HSAEC1-KT), which were established by infecting primary cultured human small airway epithelial cells with human telomerase (h*TERT*) and mouse cyclin-dependent kinase 4 (*Cdk4*) (Ramirez et al., 2004). We found that introducing *BTC* into the HSAEC1-KT cells conferred a growth advantage under anchorage-independent conditions compared to the cells with the empty vector based on their survival under detached conditions (Figure 5D). However, *BTC* expression in immortalized HSAEC1-KT cells was not sufficient for tumor formation in mice, which is consistent with the observation that human tumors require multiple genetic hits to become fully transformed. Collectively, these results demonstrate that ectopic *BTC* expression can promote both transformation of mouse cells and anchorage-independent proliferation of immortalized human lung epithelial cells.

BTC is necessary for EGFR-mutant LUAD tumor cell growth

We next asked whether BTC is also necessary for EGFR-mutant LUAD growth in cell culture and in mice. To this end, we knocked down *BTC* in EGFR mutant cell lines (PC9 and HCC2935) using *BTC* shRNAs and compared them to control cells expressing a non-specific (NS) shRNA in both soft agar assays and in a xenograft mouse model. Knockdown of *BTC* in EGFR-mutant LUAD cells resulted in reduced colony size and number in soft agar assays, indicating a reduction in growth (Figures 5E, 5F, 5H, and 5I). Consistent with these results, introduction of EGFR-mutant LUAD cells (either PC9 or HCC2935) expressing *BTC* shRNA into the flank of immunodeficient mice resulted in reduced tumor growth compared to the NS shRNA controls (Figures 5G and 5J).

We then asked whether the effect of *BTC* knockdown on growth was specific for EGFR-mutant LUAD cells by knocking down *BTC* expression in two KRAS-mutant LUAD cell lines, NCI-H358 and H460, and testing their ability to grow in an anchorage-independent manner in a soft agar assay. In contrast to EGFR mutant cells, knockdown of *BTC* in the KRAS-mutant LUAD cells did not inhibit their growth in soft agar (Figures S4A–S4D). Similarly, we tested the effect of BTC knockdown in KRAS/EGFR-wildtype LUAD cell line H1437, and in this context, we again saw no inhibition of cell growth in soft agar assays after *BTC* knockdown (Figures S4E and S4F). These results demonstrate that BTC is necessary for anchorage-independent growth of EGFR-mutant but not KRAS-mutant or EGFR/KRAS wild-type LUAD cells.

BTC loss results in reduced EGFR phosphorylation and increased apoptosis induction, resulting in growth inhibition of EGFR-mutant LUAD cells

BTC belongs to the epidermal growth factor (EGF) family of peptide ligands (Watanabe et al., 1994) that can stimulate EGFR signaling. Therefore, we asked whether ectopic expression of *BTC* enhances EGFR signaling in NIH3T3 and immortalized HSAEC1-KT cells, as indicated by an increase in phosphorylated EGFR (*p*-EGFR). We found that *BTC*-overexpressing NIH3T3 and immortalized HSAEC1-KT cells had higher *p*-EGFR levels than control cells (Figures 6A and 6B). Similarly, treatment of immortalized HSAEC1-KT cells with recombinant BTC enhanced EGFR signaling and colony formation in these cells (Figures S5A and S5B).

Conversely, PC9 and HCC2935 LUAD cells expressing *BTC* shRNAs, but not NS shRNA, had reduced *p*-EGFR levels, indicating a dampening of EGFR signaling. Notably, and consistent with the findings in NIH3T3 cells, *BTC* shRNA-expressing EGFR-mutant LUAD cells also had reduced *p*-EGFR levels (Figures 6C and 6D). Similarly, treatment with anti-BTC antibody resulted in reduced *p*-EGFR level and reduced colony formation for EGFR mutant PC9 cells (Figures S5C and S5D).

This effect was specific to EGFR-mutant LUAD cancers, as KRAS-mutant LUAD cells (H460 and H358) and EGFR/KRAS-wildtype cells (H1437) and expressing *BTC* shRNA did not show reduced EGFR signaling

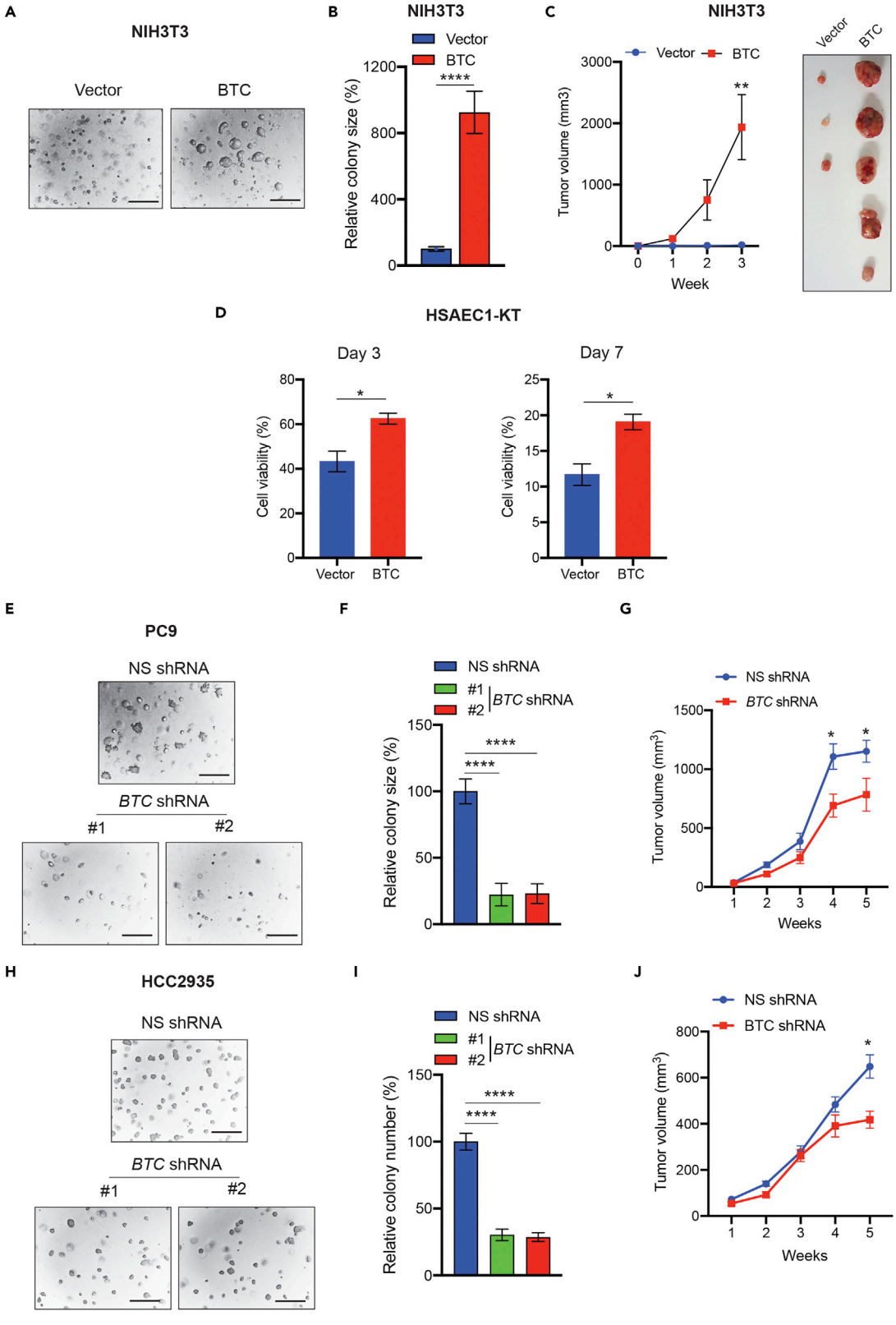
A
NIH3T3
Vector
BTC
B
NIH3T3
Vector
BTC
****
Relative colony size (%)
1200
800
400
0
C
NIH3T3
Vector
BTC
**
Tumor volume (mm3)
3000
2000
1000
0
0
1
2
3
Week
Vector
BTC
D
HSAEC1-KT
Day 3
*
Cell viability (%)
80
60
40
20
0
Vector
BTC
Day 7
*
Cell viability (%)
25
20
15
10
5
0
Vector
BTC
E
PC9
NS shRNA
BTC shRNA
#1
#2
F
NS shRNA
#1
#2
BTC shRNA
****
****
Relative colony size (%)
150
100
50
0
G
NS shRNA
BTC shRNA
*
*
Tumor volume (mm3)
1500
1000
500
0
1
2
3
4
5
Weeks
H
HCC2935
NS shRNA
BTC shRNA
#1
#2
I
NS shRNA
#1
#2
BTC shRNA
****
****
Relative colony number (%)
150
100
50
0
J
NS shRNA
BTC shRNA
*
Tumor volume (mm3)
800
600
400
200
0
1
2
3
4
5
Weeks

Figure 5. BTC expression is sufficient for tumor initiation and proliferation of immortalized human HSAEC1-KT cells

(A) NIH3T3 cells expressing either empty vector or V5-tagged *BTC* ORF were analyzed for anchorage-independent growth in a soft agar assay. Representative images are shown. Scale bar, 200 μm.

(B) Relative colony size (%) for the soft agar data shown in panel (A).

(C) NIH3T3 cells expressing either vector or V5-tagged *BTC* ORF were injected subcutaneously into the flank of athymic nude mice (n = 5). Tumor volumes at the indicated times (left) and tumor images (right) are shown.

(D) HSAEC1-KT cells expressing empty vector or the V5-tagged *BTC* ORF were analyzed for survival under detached conditions in ultra-low attachment plates. The percentage of surviving cells at days 3 and 7 of culture under the indicated conditions is shown.

(E) PC9 cells expressing *BTC* shRNAs or a control non-silencing (NS) shRNA were analyzed for anchorage-independent growth in soft agar assays. Representative images are shown. Scale bar, 200 μm.

(F) Relative colony size for the soft agar data shown in panel (E).

(G) PC9 cells expressing either *BTC* shRNA or NS shRNA were injected subcutaneously into the flank of NSG mice (n = 10). Tumor volumes at the indicated times are shown.

(H) HCC2935 cells expressing *BTC* shRNAs or a control NS shRNA were analyzed for anchorage-independent growth in soft agar assays. Representative images are shown. Scale bar: 200 μm.

(I) Relative colony number for the soft agar data shown in panel (H).

(J) HCC2935 cells expressing either *BTC* shRNA or NS shRNA were injected subcutaneously into the flank of NSG mice (n = 10). Tumor volumes at the indicated times (left) and tumor images (right) are shown. Data are shown as the mean ± SEM, *p<0.05, **p<0.01, ****p<0.0001. See also Figures S4 and S5.

(Figures S5E–S5G). Similarly, the treatment of *KRAS*-mutant LUAD cells (H460 and H358) and *EGFR*/*KRAS*–wild-type cells (H1437) with anti-BTC antibody did not inhibit their colony formation abilities (Figures S5H–S5J).

In addition to binding EGFR, BTC can also bind to and activate ERBB4 homodimers (Beerli and Hynes, 1996; Riese et al., 1996) and all possible combinations of ERBB heterodimers, including the highly oncogenic ERBB2/3 dimer (Alimandi et al., 1997; Pinkas-Kramarski et al., 1998). Consequently, BTC has been classified as a pan-ERBB ligand (Pinkas-Kramarski et al., 1998). To assess the impact of BTC expression on the phosphorylation of other receptor tyrosine kinases, we used whole cell lysates and phosphorylated receptor tyrosine kinase (RTK) arrays to monitor changes in RTK phosphorylation in response to both increased and decreased *BTC* expression. To monitor the effect of increased expression, we used whole-cell lysates from NIH3T3 cells expressing *BTC* and a mouse RTK array that monitors changes in the phosphorylation of 39 different mouse RTKs. We found that NIH3T3 cells ectopically expressing *BTC* had significant increases in EGFR and ERBB2 phosphorylation compared to empty vector controls (Figures 6E and 6F). To monitor the effect of decreased *BTC* expression, we used PC9 cells expressing *BTC* shRNAs and a human RTK array that monitors changes in the phosphorylation of 49 different human receptor tyrosine kinases. Our results showed that knockdown of *BTC* in PC9 cells strongly inhibited the phosphorylation of EGFR, ERBB2 and ERBB3 (Figures 6G and 6H).

Previous studies have shown that BTC can bind EGF receptors and induce dimerization with other ERBB family members (Dahlhoff et al., 2014; Dunbar and Goddard, 2000; Jones et al., 1999; Rush et al., 2018). Therefore, we analyzed NIH3T3 cells ectopically expressing *BTC* or PC9 cells with *BTC* shRNA for possible BTC-induced phosphorylation of EGFR and ERBB2 and/or ERBB3 by immunoprecipitation analysis. NIH3T3 cells expressing empty vector or PC9 cells expressing non-specific shRNAs were used as controls. We performed phosphotyrosine immunoprecipitation and measured the relative levels of immunoprecipitated EGFR, ERBB2, and ERBB3. We found that, in the presence of BTC, phosphorylation of EGFR and ERBB2 increased (Figure S6).

Based on these results, we asked whether ERBB2 or ERBB3 is important for the growth of EGFR-mutant LUAD cells by knocking down the expression of *ERBB2* and *ERBB3* in PC9 cells and testing their ability to form colonies in soft agar and tumors in mice. Knockdown of *ERBB2* or *ERBB3* did not affect the ability of PC9 cells to form colonies in soft agar or tumors in mice (Figure S7). Collectively, these results show that BTC enhances EGFR signaling to cause cellular transformation and promote tumor growth that is not dependent on ERBB2 and ERBB3.

Because we observed that BTC knockdown reduced tumor growth in EGFR mutant cell lines, we next explored the contribution of both wild-type and mutant EGFR to mediating the cancer-promoting activity of BTC. To this end, we performed two sets of experiments. First, we treated NIH3T3 cells expressing vector, wild-type EGFR, or different mutants of EGFR (EGFR L858R, EGFR L861Q, and EGFR DEL1). We found that BTC induced not only the wild-type EGFR but also phosphorylation at several sites of mutant EGFR

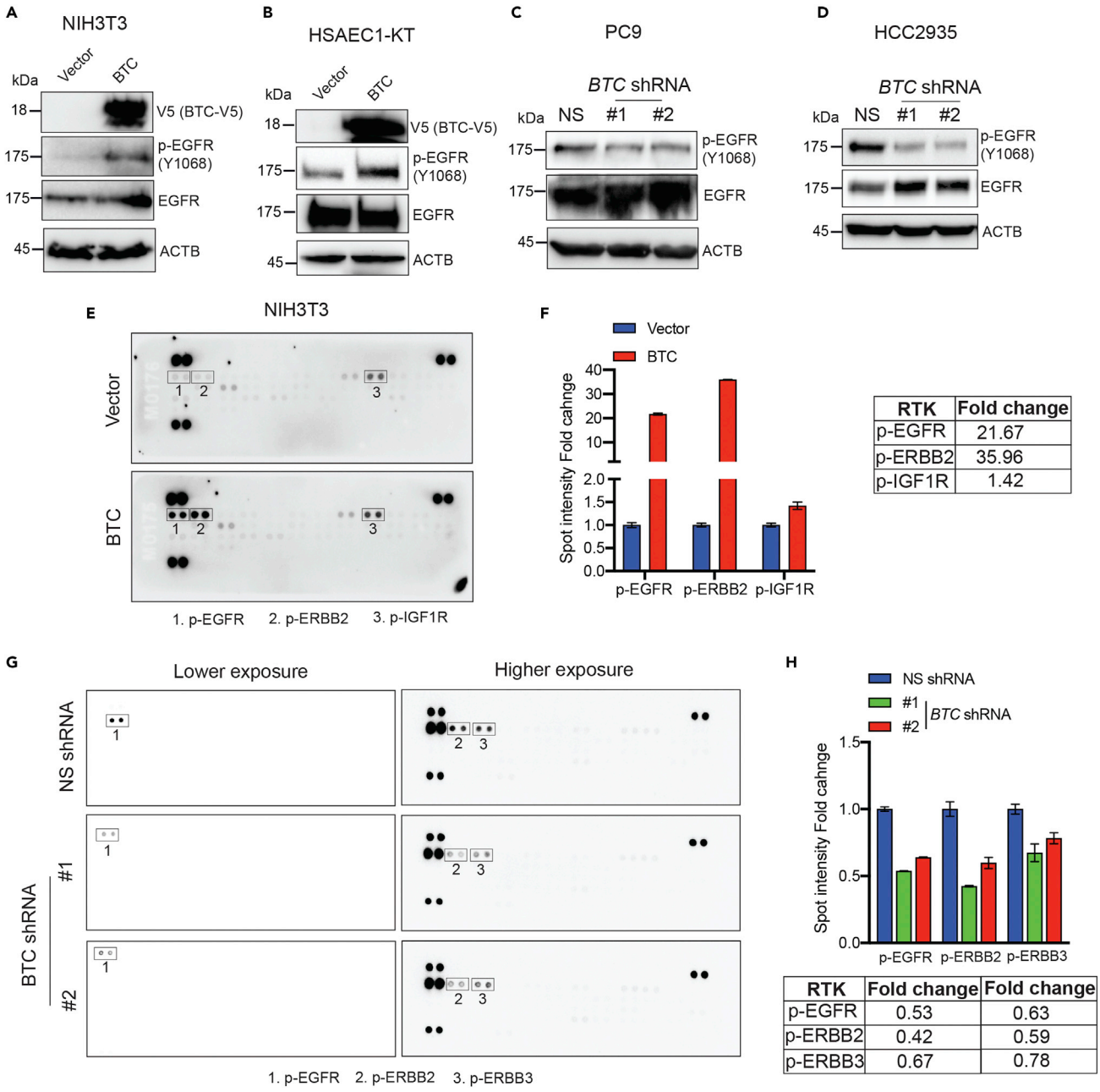

Figure 6. BTC is both necessary and sufficient to stimulate EGFR signaling

(A) NIH3T3 cells expressing either empty vector or the V5-tagged *BTC* ORF were analyzed for the indicated proteins by immunoblotting. ACTB was used as a loading control.

(B) HSAEC1-KT cells expressing either empty vector or the V5-tagged *BTC* ORF were analyzed for the indicated proteins by immunoblotting. ACTB was used as a loading control.

(C) PC9 cells expressing either a non-silencing shRNA or *BTC* shRNA were analyzed for indicated proteins by immunoblotting. ACTB was used as a loading control.

(D) HCC2935 cells expressing either a non-silencing shRNA or *BTC* shRNA were analyzed for indicated proteins by immunoblotting. ACTB was used as a loading control.

(E) Proteome Profiler Mouse Phospho-RTK Array membranes were incubated with lysates from NIH3T3 cells expressing either empty vector or V5-tagged *BTC* ORF. Array membranes incubated with lysates from vector or V5-tagged *BTC* ORF is shown.

(F) Quantification of *p*-EGFR, *p*-ERBB2 and *p*-IGF1R for data shown in (E).

(G) Proteome Profiler Human Phospho-RTK Array membranes showing relative RTK phosphorylation in PC9 cells expressing NS or *BTC* specific shRNAs is shown.

(H) Quantification of *p*-EGFR, *p*-ERBB2 and *p*-ERBB3 for data shown in panel (G). Data are shown as the mean ±SEM See also Figures S6 and S7.

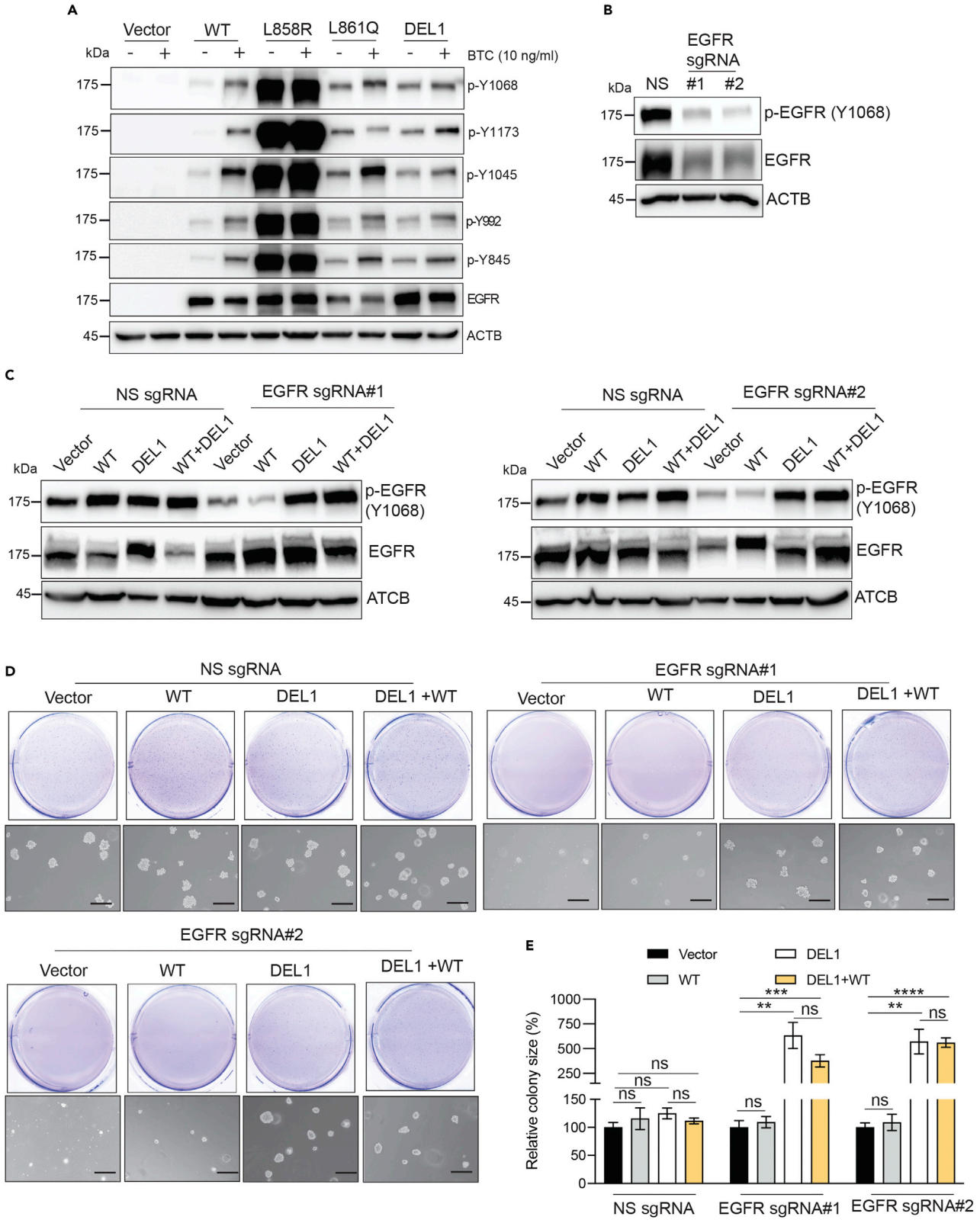
A
Vector
WT
L858R
L861Q
DEL1
kDa
BTC (10 ng/ml)
p-Y1068
p-Y1173
p-Y1045
p-Y992
p-Y845
EGFR
ACTB
B
EGFR sgRNA
NS
#1
#2
p-EGFR (Y1068)
EGFR
ACTB
C
NS sgRNA
EGFR sgRNA#1
EGFR sgRNA#2
Vector
WT
DEL1
WT+DEL1
p-EGFR (Y1068)
EGFR
ATCB
D
NS sgRNA
EGFR sgRNA#1
EGFR sgRNA#2
Vector
WT
DEL1
DEL1 +WT
E
Vector
WT
DEL1
DEL1+WT
Relative colony size (%)
ns
**
***
****
NS sgRNA
EGFR sgRNA#1
EGFR sgRNA#2

Figure 7. BTC stimulates phosphorylation of mutant EGFR, and only mutant, but not wild-type, EGFR can induce transformation

(A) NIH3T3 cells expressing empty vector, wild-type EGFR, or the indicated EGFR mutants were serum-starved for 12 h. They were then stimulated with BTC (10 ng/mL) for 30 min and analyzed for the indicated EGFR phosphorylation sites. Total EGFR and ACTB were used as loading control.

(B) PC9 cells were infected with lentiviral particles expressing non-specific (NS) sgRNA or two sequence-independent EGFR sgRNAs. Immunoblotting for phosho-EGFR, total EGFR, and ACTB is shown.

(C) PC9 cells with NS or EGFR sgRNAs were infected with empty vector or wild-type or mutant EGFR and analyzed for the indicated proteins by immunoblotting. ACTB was used as a loading control.

(D) PC9 cells with NS or EGFR sgRNAs were infected with empty vector or wild-type or mutant EGFR or both wild-type and mutant EGFR and analyzed in a soft agar assay. Representative images of the well and microscopic images are shown. Scale bar, 200 μm.

(E) Relative colony size for the data presented in panel (D). Data are shown as the mean ±SEM ns = not significant, **p<0.01, ***p<0.001, ****p<0.0001.

(Figure 7A). Next, to more clearly evaluate the impact of wild-type versus mutant EGFR in cellular transformation, we knocked out expression of EGFR in EGFR-mutant PC9 cells using a CRISPR-based gene knockout approach (Figure 7B). These cells were then reconstituted with either wild-type or DEL1-mutant EGFR or both (Figure 7C). We found that sgRNA-induced deletion of EGFR prevented PC9 cells from forming colonies in a soft agar assay compared to PC9 cells expressing a control non-specific (NS) sgRNA (Figures 7D and 7E). Furthermore, ectopic expression of EGFR-DEL1 mutation restored the soft agar colony-forming ability of PC9 cells, but wild-type EGFR failed to do so (Figures 7D and 7E). However, PC9 cells co-expressing wild-type EGFR and EGFR-DEL1 did not form significantly larger colonies compared to EGFR-DEL1-expressing cells (Figures 7D and 7E). These results indicate that BTC can in part function to promote tumor growth by activating mutant EGFR, although this could be a context-specific phenomenon, as we also observed that BTC could transform wild-type EGFR-expressing NIH3T3 cells (Figures 5A–5C) and increase the proliferation of HSAEC1-KT1 cells (Figure 5D).

Next, we assessed the cellular consequences of reduced EGFR signaling because of *BTC* knockdown. Previous studies have shown that attenuation of oncogenic signaling can result in apoptosis induction (Costa et al., 2007; Faber et al., 2009). Therefore, we asked whether ectopic expression of *BTC* leads to apoptosis resistance, and conversely, whether knockdown of *BTC* leads to increased apoptosis induction by measuring cleaved caspase 3. As expected, knockdown of *BTC* resulted in increased levels of cleaved caspase 3 (Figures 8A and 8B), whereas *BTC* overexpression resulted in reduced levels of cleaved caspase 3 (Figure 8C) in cells grown under detached conditions. To further confirm the role of BTC in suppressing apoptosis, we measured apoptosis using annexin V staining. Consistent with the role of BTC in suppressing apoptosis, BTC knockdown EGFR mutant LUAD cells showed increased annexin V staining (Figures 8D and 8E). Taken together, these results demonstrate that BTC enhances EGFR signaling and an anti-apoptotic response to promote tumor development and LUAD tumor growth.

DISCUSSION

The Cancer Genome Atlas study has identified 45 distinct *EGFR* mutations in LUAD (Cancer Genome Atlas Research Network, 2014), and these mutations are present in approximately 15% of LUADs. Oncogenic *EGFR* mutations provide an actionable target for treating this genetic subtype of LUAD using clinically efficacious EGFR-TKIs (Herbst et al., 2018). However, not all *EGFR*-mutant LUAD patients respond to EGFR-TKIs, and many of those who show an initial response eventually fail therapy because of the emergence of acquired resistance (Gainor and Shaw, 2013; Roper et al., 2020). Therefore, a better understanding of *EGFR*-mutant LUAD is necessary to identify additional druggable targets to more effectively treat patients with this disease. Here, we tested the effects of three frequently occurring LUAD-associated *EGFR* mutants on mRNA expression in an attempt to identify new regulators of EGFR-driven tumor growth. For each *EGFR* mutant tested, we identified several genes with altered expression patterns that grouped into the same top pathways, indicating a significantly shared transcriptional signature among LUAD-associated *EGFR* mutations, each of which was sufficient to achieve cellular transformation, which in part explains the mutual exclusivity of various EGFR mutations.

One upregulated gene in all three of the EGFR mutants was *BTC*. BTC belongs to the epidermal growth factor (EGF) family of peptide ligands (Watanabe et al., 1994) and can bind to and activate not only EGFR, but also ERBB4 homodimers (Beerli and Hynes, 1996; Riese et al., 1996), and all possible combinations of ERBB heterodimers, including the highly oncogenic ERBB2/3 dimer (Alimandi et al., 1997; Pinkas-Kramarski et al., 1998). Based on these findings, BTC has been classified as a pan-ERBB ligand (Pinkas-Kramarski et al., 1998).

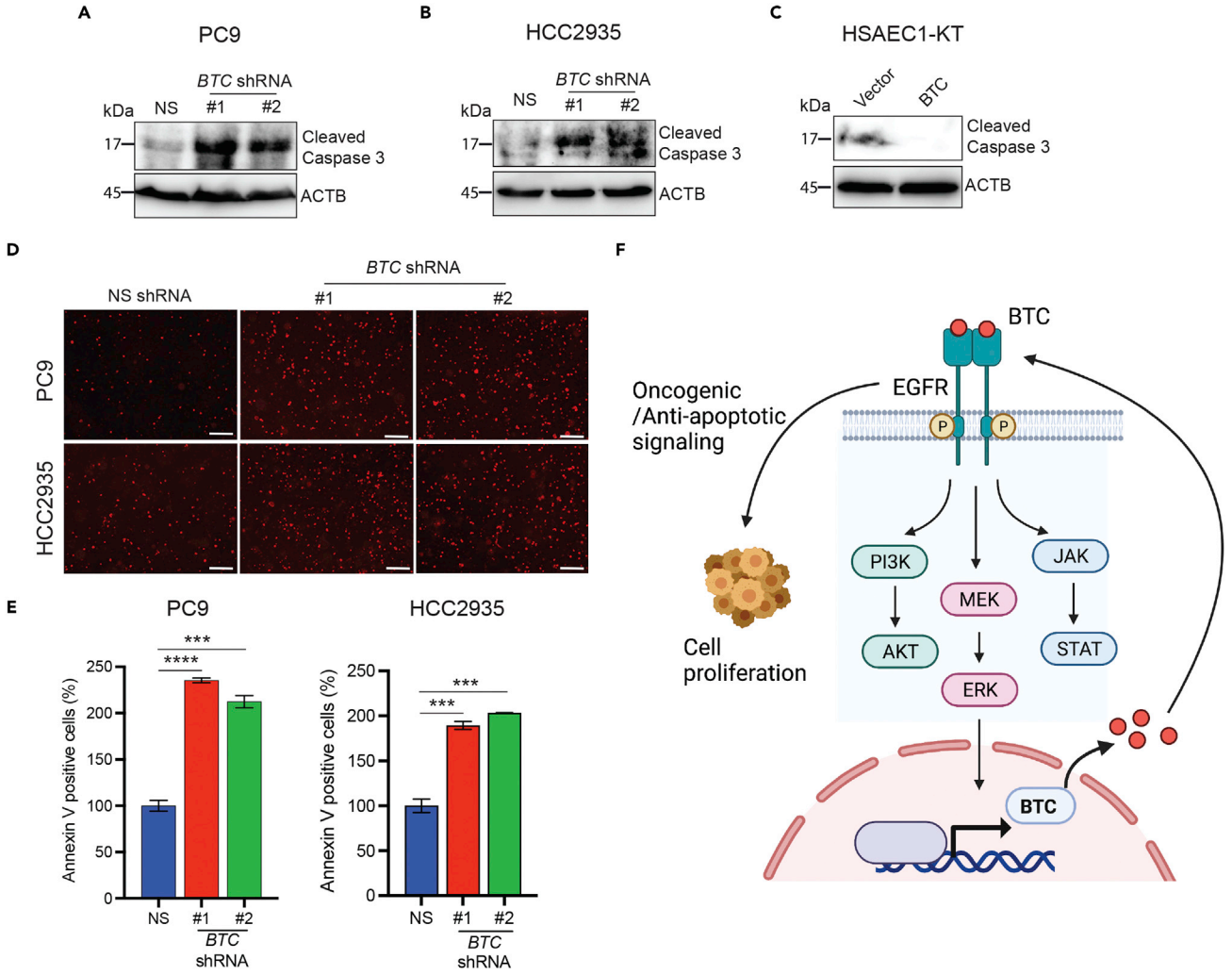

Figure 8. BTC attenuates apoptosisinduction

(A) PC9 cells expressing non-specific (NS) or *BTC* shRNAs were analyzed for cleaved caspase three using immunoblotting analysis. ACTB was used as a loading control.

(B) HCC2935 cells expressing NS or *BTC* shRNAs were analyzed for cleaved caspase three using immunoblotting analysis. ACTB was used as a loading control.

(C) HSAEC1-KT cells expressing vector or the V5-tagged *BTC* ORF were analyzed for cleaved caspase three using immunoblotting analysis. ACTB was used as a loading control.

(D) PC9 and HCC2935 cells expressing NS or BTC shRNAs were analyzed for annexin V-positive cells. Representative micrographs are shown. Scale bar, 200 μm.

(E) Quantitation of the annexin V-positive cells under the indicated conditions for the experiment shown in panel (D).

(F) Model showing the mechanism of BTC action in EGFR mutant lung adenocarcinoma. Data are shown as the mean ±SEM ***p<0.001, ****p<0.0001.

Previous studies have shown that seven different ligands can bind to and activate EGFR, including epidermal growth factor-alpha (EGFα), transforming growth factor α (TGFα), heparin-binding EGF-like growth factor (HBEGF), betacellulin (BTC), amphiregulin (AREG), epiregulin (EREG), and epigen (EPGN) (Singh et al., 2016). Among these ligands, BTC, EGF, TGFA, and HBEGF are considered high-affinity ligands, whereas AREG, EREG, and EPGN are considered low-affinity ligands (Singh et al., 2016). We found that mutant EGFR significantly upregulated the expression of BTC and established that it was the direct target of mutant EGFR signaling, as treatment with erlotinib, an EGFR TKI, inhibited the expression of BTC in cells expressing EGFR mutant proteins (Figure 8F). These studies also revealed a positive feedback loop in which EGFR transcriptionally activates BTC, which, in turn, stimulates EGFR signaling.

Mutations in EGFR can activate multiple downstream signaling pathways that promote cancer cell proliferation and survival. These include the MAPK, PI3K, and JAK/STAT pathways, which play various roles downstream of EGFR signaling (Bromberg, 2002). MAPK signaling plays an important role in regulating cellular proliferation and survival. Activated MAPKs are translocated to the nucleus, where they phosphorylate specific transcription factors involved in cell proliferation (Gaestel, 2006; Hill and Treisman, 1995). These transcription factors, in turn, mediate the transcriptional activity of the MAPK pathway. We showed that mutant EGFR engaged and activated the downstream MEK–ERK pathway, causing activation of BTC expression. We also showed that BTC is clinically relevant to LUAD, as a large percentage of LUAD samples included on tissue microarrays appear to overexpress BTC, with a slightly higher percentage of *EGFR*-mutant LUADs showing strong BTC expression than other LUADs.

However, BTC expression was also higher in *KRAS*-mutant and *EGFR*/*KRAS*–wild-type LUAD, likely associated with increased MAPK activity because of *KRAS* mutations or other MAPK pathway activating events in *EGFR*/*KRAS*–wild-type LUAD. However, our functional studies using BTC shRNAs demonstrated that BTC did not play a tumor-promoting role in *KRAS*-mutant and *EGFR*/*KRAS*–wild-type LUAD. These observations further strengthen our argument that BTC primarily exerts its tumor-promoting activity via the stimulation of EGFR signaling and are consistent with the literature that EGFR signaling is not required for oncogenic *KRAS*-driven LUAD tumor growth or for *EGFR*/*KRAS*–wild-type LUAD tumor growth.

BTC plays an important role in cancer. For example, BTC induces Slug-mediated downregulation of E-cadherin and cell migration in ovarian cancer cells (Zhao et al., 2016) and also enhances ovarian cancer cell migration by upregulating Connexin43 via MEK-ERK signaling (Zhao et al., 2020). In addition, BTC is overexpressed in pancreatic cancer and hepatocellular carcinoma (Moon et al., 2006; Yokoyama et al., 1995). We have shown that ectopic expression of *BTC* is sufficient to transform immortalized mouse NIH3T3 cells and promote the survival of, but not the transformation of, immortalized HSAEC1-KT cells. The inability of *BTC* alone to transform immortalized human HSAEC1-KT cells is not surprising: human cell transformation is much more complex and requires many more genetic/epigenetic alterations to be fully transformed compared to immortalized mouse cells. Therefore, our findings are consistent with the literature, which describes significant differences between human and mouse cells in their abilities to initiate tumor development (Hamad et al., 2002; Rangarajan and Weinberg, 2003). Furthermore, we found that *BTC* knockdown resulted in increased apoptosis induction, suggesting that EGFR pathway activation via BTC promotes EGFR pathway–driven tumor cell survival, resulting in enhanced tumor growth and progression. Our findings demonstrating that BTC promotes an anti-apoptotic state are consistent with previous reports suggesting that BTC promotes such phenotypes in a variety of tumors and contexts (Fan et al., 2020; Shi et al., 2014; Yilmaz et al., 2011). Furthermore, BTC was also shown to have a greater inhibitory effect on apoptosis induction than other EGFR ligands, such as EGF (Saito et al., 2004).

Finally, our studies using a BTC-neutralizing antibody highlighted the exciting possibility of targeting BTC for treating *EGFR*-mutant LUAD. This possibility is further supported by another study in glioblastoma (GBM), which showed that a BTC-neutralizing antibody abrogated the activation of both EGFR and NF-κB in response to STAT3 inhibition and that the combined blockade of STAT3 and BTC induced apoptosis in GBM cells (Fan et al., 2020). Collectively, these results demonstrate that BTC drives growth in *EGFR*-mutant lung cancer and warrants further evaluation as a therapeutic target in *EGFR*-mutant LUAD.

Limitations of the study

In this study, we used NIH3T3-based model system to identity factors necessary for oncogenic EGFR-driven tumor development and progression. Although, we have established the utility of this model by demonstrating the role of BTC in EGFR mutant LUAD using multiple human relevant model systems, including human LUAD cell lines, xenograft-based mouse models of human LUAD and human patient-derived LUAD samples. However, it is possible that some other genes that would have been identified as oncogenic EGFR targets in a human lung epithelial-cell-based model system were not identified in NIH3T3-based mouse cell line model system. A future study that compares our model system with that of human lung epithelial-cell-based model of EGFR-driven tumor development and progression may be able to identity such differences. Another interesting observation that we made was that not all genes that were altered as

a result of introducing EGFR mutations in NIH3T3 cells were direct targets of oncogenic EGFR signaling. This raises an exiciting possibility of stochastic gene expression changes because of the EGFR mutations. The roles of these genes, if any, in the context of EGFR mutant LUAD were not tested and would be important to analyze for fully understanding the mechanism of oncogenic EGFR-driven tumor development and progression.

STAR★METHODS

Detailed methods are provided in the online version of this paper and include the following:

- KEY RESOURCES TABLE
- RESOURCE AVAILABILITY
  - Lead contact
  - Materials availability
  - Data and code availability
- EXPERIMENTAL MODEL AND SUBJECT DETAILS
  - Cell culture
  - Mouse tumorigenesis experiments
- METHOD DETAILS
  - Plasmids and preparation of the lentiviral and retroviral stable cell lines
  - RNA preparation, cDNA synthesis, and RT-qPCR analysis
  - Immunoblotting
  - MTT assays
  - Soft agar assay
  - RNA-seq and data analysis
  - Immunohistochemistry
  - Mouse RTK arrays
  - Human RTK arrays
  - Immunoprecipitation
  - Cell viability assay in ultra-low attachment plates
  - Annexin V assay
- QUANTIFICATION AND STATISTICAL ANALYSIS

SUPPLEMENTAL INFORMATION

Supplemental information can be found online at https://doi.org/10.1016/j.isci.2022.104211.

ACKNOWLEDGMENTS

We thank Prof. David Rimm and Dr. Maria Toki, Department of Pathology at Yale University, for providing the tissue microarray YTMA 310 for our studies. We gratefully acknowledge grants from the National Institutes of Health: R01CA195077-01A1 (N.W.), R01CA200919-01 (N.W.), and R01 CA218008-01A1 (N.W.), R03 CA230815 (R.G.) R03CA248913 (R.G.) and R01CA233481 (R.G.).

AUTHOR CONTRIBUTIONS

S.C., S.B., R.G., and N.W. conceived and designed the experiments. S.C. performed most of the experiments with help from S.B. X.Z. analyzed and scored the BTC immunohistochemistry data. S.C., R.G., and N.W. prepared the figures and co-wrote the manuscript. All authors read and commented on the paper and approved the final manuscript.

DECLARATION OF INTERESTS

The authors declare no competing interests.

Received: December 10, 2021
Revised: March 18, 2022
Accepted: April 4, 2022
Published: May 20, 2022

REFERENCES

Alimandi, M., Wang, L.M., Bottaro, D., Lee, C.C., Kuo, A., Frankel, M., Fedi, P., Tang, C., Lippman, M., and Pierce, J.H. (1997). Epidermal growth factor and betacellulin mediate signal transduction through co-expressed ErbB2 and ErbB3 receptors. EMBO J. *16*, 5608–5617.

Beerli, R.R., and Hynes, N.E. (1996). Epidermal growth factor-related peptides activate distinct subsets of ErbB receptors and differ in their biological activities. J. Biol. Chem. *271*, 6071–6076.

Boehm, J.S., Zhao, J.J., Yao, J., Kim, S.Y., Firestein, R., Dunn, I.F., Sjostrom, S.K., Garraway, L.A., Weremowicz, S., Richardson, A.L., et al. (2007). Integrative genomic approaches identify IKBKE as a breast cancer oncogene. Cell *129*, 1065–1079.

Bray, F., Ferlay, J., Soerjomataram, I., Siegel, R.L., Torre, L.A., and Jemal, A. (2018). Global cancer statistics 2018: GLOBOCAN estimates of incidence and mortality worldwide for 36 cancers in 185 countries. CA Cancer J. Clin. *68*, 394–424.

Bromberg, J. (2002). Stat proteins and oncogenesis. J. Clin. Invest. *109*, 1139–1142.

Cancer Genome Atlas Research Network (2014). Comprehensive molecular profiling of lung adenocarcinoma. Nature *511*, 543–550.

Chen, D., Li, Y., Wang, L., and Jiao, K. (2015). SEMA6D expression and patient survival in breast invasive carcinoma. Int. J. Breast Cancer *2015*, 539721.

Costa, D.B., Halmos, B., Kumar, A., Schumer, S.T., Huberman, M.S., Boggon, T.J., Tenen, D.G., and Kobayashi, S. (2007). BIM mediates EGFR tyrosine kinase inhibitor-induced apoptosis in lung cancers with oncogenic EGFR mutations. PLoS Med. *4*, 1669–1679, discussion 1680.

Dahlhoff, M., Wolf, E., and Schneider, M.R. (2014). The ABC of BTC: structural properties and biological roles of betacellulin. Semin.Cell Dev. Biol. *28*, 42–48.

Dela Cruz, C.S., Tanoue, L.T., and Matthay, R.A. (2011). Lung cancer: epidemiology, etiology, and prevention. Clin. Chest Med. *32*, 605–644.

Ding, L., Getz, G., Wheeler, D.A., Mardis, E.R., McLellan, M.D., Cibulskis, K., Sougnez, C., Greulich, H., Muzny, D.M., Morgan, M.B., et al. (2008). Somatic mutations affect key pathways in lung adenocarcinoma. Nature *455*, 1069–1075.

Dunbar, A.J., and Goddard, C. (2000). Structure-function and biological role of betacellulin. Int. J. Biochem. Cell Biol. *32*, 805–815.

Faber, A.C., Li, D., Song, Y., Liang, M.C., Yeap, B.Y., Bronson, R.T., Lifshits, E., Chen, Z., Maira, S.M., Garcia-Echeverria, C., et al. (2009). Differential induction of apoptosis in HER2 and EGFR addicted cancers following PI3K inhibition. Proc. Natl. Acad. Sci. U S A *106*, 19503–19508.

Fan, Q., An, Z., Wong, R.A., Luo, X., Lu, E.D., Baldwin, A., Mayekar, M.K., Haderk, F., Shokat, K.M., Bivona, T.G., et al. (2020). Betacellulin drives therapy resistance in glioblastoma. Neuro Oncol. *22*, 457–469.

Gaestel, M. (2006). MAPKAP kinases - MKs - two's company, three's a crowd. Nat. Rev. Mol. Cell Biol. *7*, 120–130.

Gainor, J.F., and Shaw, A.T. (2013). Emerging paradigms in the development of resistance to tyrosine kinase inhibitors in lung cancer. J. Clin. Oncol. *31*, 3987–3996.

Govindan, R., Ding, L., Griffith, M., Subramanian, J., Dees, N.D., Kanchi, K.L., Maher, C.A., Fulton, R., Fulton, L., Wallis, J., et al. (2012). Genomic landscape of non-small cell lung cancer in smokers and never-smokers. Cell *150*, 1121–1134.

Hamad, N.M., Elconin, J.H., Karnoub, A.E., Bai, W., Rich, J.N., Abraham, R.T., Der, C.J., and Counter, C.M. (2002). Distinct requirements for Ras oncogenesis in human versus mouse cells. Genes Dev. *16*, 2045–2057.

Herbst, R.S., Morgensztern, D., and Boshoff, C. (2018). The biology and management of non-small cell lung cancer. Nature *553*, 446–454.

Hill, C.S., and Treisman, R. (1995). Transcriptional regulation by extracellular signals: mechanisms and specificity. Cell *80*, 199–211.

Hu, S., and Zhu, L. (2018). Semaphorins and their receptors: from axonal guidance to atherosclerosis. Front. Physiol. *9*, 1236.

Jones, J.T., Akita, R.W., and Sliwkowski, M.X. (1999). Binding specificities and affinities of egf domains for ErbB receptors. FEBS Lett. *447*, 227–231.

Khelwatty, S., Essapen, S., Bagwan, I., Green, M., Seddon, A., and Modjtahedi, H. (2017). The impact of co-expression of wild-type EGFR and its ligands determined by immunohistochemistry for response to treatment with cetuximab in patients with metastatic colorectal cancer. Oncotarget *8*, 7666–7677.

Kim, Y.J., Jang, W., Piao, X.M., Yoon, H.Y., Byun, Y.J., Kim, J.S., Kim, S.M., Lee, S.K., Seo, S.P., Kang, H.W., et al. (2019). ZNF492 and GPR149 methylation patterns as prognostic markers for clear cell renal cell carcinoma: arraybased DNA methylation profiling. Oncol. Rep. *42*, 453–460.

Kinehara, Y., Nagatomo, I., Koyama, S., Ito, D., Nojima, S., Kurebayashi, R., Nakanishi, Y., Suga, Y., Nishijima-Futami, Y., Osa, A., et al. (2018). Semaphorin 7A promotes EGFR-TKI resistance in EGFR mutant lung adenocarcinoma cells. JCI Insight *3*, e123093.

Li, S., Yang, F., Yang, Y.K., and Zhou, Y. (2019). Increased expression of ecotropic viral integration site 2A indicates a poor prognosis and promotes osteosarcoma evolution through activating MEK/ERK pathway. J. Recept. Signal Transduct. Res. *39*, 368–372.

Li, P., Lv, H., Xu, M., Zang, B., and Ma, Y. (2020). ARHGAP6 promotes apoptosis and inhibits glycolysis in lung adenocarcinoma through STAT3 signaling pathway. Cancer Manag. Res. *12*, 9665–9678.

Moon, W.S., Park, H.S., Yu, K.H., Park, M.Y., Kim, K.R., Jang, K.Y., Kim, J.S., and Cho, B.H. (2006). Expression of betacellulin and epidermal growth factor receptor in hepatocellular carcinoma: implications for angiogenesis. Hum. Pathol. *37*, 1324–1332.

Pinkas-Kramarski, R., Lenferink, A.E., Bacus, S.S., Lyass, L., van de Poll, M.L., Klapper, L.N., Tzahar, E., Sela, M., van Zoelen, E.J., and Yarden, Y. (1998). The oncogenic ErbB-2/ErbB-3 heterodimer is a surrogate receptor of the epidermal growth factor and betacellulin. Oncogene *16*, 1249–1258.

Ramirez, R.D., Sheridan, S., Girard, L., Sato, M., Kim, Y., Pollack, J., Peyton, M., Zou, Y., Kurie, J.M., Dimaio, J.M., et al. (2004). Immortalization of human bronchial epithelial cells in the absence of viral oncoproteins. Cancer Res. *64*, 9027–9034.

Rangarajan, A., and Weinberg, R.A. (2003). Opinion: comparative biology of mouse versus human cells: modelling human cancer in mice. Nat. Rev. Cancer *3*, 952–959.

Rau, K.M., Chen, H.K., Shiu, L.Y., Chao, T.L., Lo, Y.P., Wang, C.C., Lin, M.C., and Huang, C.C. (2016). Discordance of mutation statuses of epidermal growth factor receptor and K-ras between primary adenocarcinoma of lung and brain metastasis. Int. J. Mol. Sci. *17*, 524.

Riese, D.J., 2nd, Bermingham, Y., van Raaij, T.M., Buckley, S., Plowman, G.D., and Stern, D.F. (1996). Betacellulin activates the epidermal growth factor receptor and erbB-4, and induces cellular response patterns distinct from those stimulated by epidermal growth factor or neuregulin-beta. Oncogene *12*, 345–353.

Roper, N., Brown, A.L., Wei, J.S., Pack, S., Trindade, C., Kim, C., Restifo, O., Gao, S., Sindiri, S., Mehrabadi, F., et al. (2020). Clonal evolution and heterogeneity of osimertinib acquired resistance mechanisms in EGFR mutant lung cancer. Cell Rep.Med. *1*, 100007.

Rush, J.S., Peterson, J.L., and Ceresa, B.P. (2018). Betacellulin (BTC) biases the EGFR to dimerize with ErbB3. Mol. Pharmacol. *94*, 1382–1390.

Saito, T., Okada, S., Ohshima, K., Yamada, E., Sato, M., Uehara, Y., Shimizu, H., Pessin, J.E., and Mori, M. (2004). Differential activation of epidermal growth factor (EGF) receptor downstream signaling pathways by betacellulin and EGF. Endocrinology *145*, 4232–4243.

Santra, M.K., Wajapeyee, N., and Green, M.R. (2009). F-box protein FBXO31 mediates cyclin D1 degradation to induce G1 arrest after DNA damage. Nature *459*, 722–725.

Shi, L., Wang, L., Wang, B., Cretoiu, S.M., Wang, Q., Wang, X., and Chen, C. (2014). Regulatory mechanisms of betacellulin in CXCL8 production from lung cancer cells. J. Transl. Med. *12*, 70.

Shing, Y., Christofori, G., Hanahan, D., Ono, Y., Sasada, R., Igarashi, K., and Folkman, J. (1993). Betacellulin: a mitogen from pancreatic beta cell tumors. Science *259*, 1604–1607.

Singh, B., and Coffey, R.J. (2014). Trafficking of epidermal growth factor receptor ligands in

polarized epithelial cells. Annu. Rev. Physiol. *76*, 275–300.

Singh, B., Carpenter, G., and Coffey, R.J. (2016). EGF receptor ligands: recent advances. F1000Research *5*, F1000 Faculty Rev-2270.

Sun, M., Behrens, C., Feng, L., Ozburn, N., Tang, X., Yin, G., Komaki, R., Varella-Garcia, M., Hong, W.K., Aldape, K.D., et al. (2009). HER family receptor abnormalities in lung cancer brain metastases and corresponding primary tumors. Clin. Cancer Res. *15*, 4829–4837.

Trapnell, C., Roberts, A., Goff, L., Pertea, G., Kim, D., Kelley, D.R., Pimentel, H., Salzberg, S.L., Rinn, J.L., and Pachter, L. (2012). Differential gene and transcript expression analysis of RNA-seq experiments with TopHat and Cufflinks. Nat. Protoc. *7*, 562–578.

Watanabe, T., Shintani, A., Nakata, M., Shing, Y., Folkman, J., Igarashi, K., and Sasada, R. (1994). Recombinant human betacellulin. Molecular structure, biological activities, and receptor interaction. J. Biol. Chem. *269*, 9966–9973.

Wu, Y., Xu, M., He, R., Xu, K., and Ma, Y. (2019). ARHGAP6 regulates the proliferation, migration and invasion of lung cancer cells. Oncol. Rep. *41*, 2281–2888.

Yarden, Y., and Sliwkowski, M.X. (2001). Untangling the ErbB signalling network. Nat. Rev. Mol. Cell Biol. *2*, 127–137.

Yilmaz, M., Maass, D., Tiwari, N., Waldmeier, L., Schmidt, P., Lehembre, F., and Christofori, G. (2011). Transcription factor Dlx2 protects from TGFbeta-induced cell-cycle arrest and apoptosis. EMBO J. *30*, 4489–4499.

Yokoyama, M., Funatomi, H., Kobrin, M., Ebert, M., Friess, H., Buchler, M., and Korc, M. (1995). Betacellulin, a member of the epidermal growth-factor family, is overexpressed in human pancreatic-cancer. Int. J. Oncol. *7*, 825–829.

Zhao, J., Klausen, C., Qiu, X., Cheng, J.C., Chang, H.M., and Leung, P.C. (2016). Betacellulin induces slug-mediated down-regulation of E-cadherin and cell migration in ovarian cancer cells. Oncotarget *7*, 28881–28890.

Zhao, J., Klausen, C., Yi, Y., Cheng, J.C., Chang, H.M., and Leung, P.C.K. (2020). Betacellulin enhances ovarian cancer cell migration by up-regulating Connexin43 via MEK-ERK signaling. Cell Signal. *65*, 109439.

STAR★METHODS

KEY RESOURCES TABLE

REAGENT or RESOURCE	SOURCE	IDENTIFIER
Antibodies		
BTC (IHC antibody)	R&D biosystems	Cat# MAB2611 RRID: AB_2067503
BTC (Neutralization antibody)	R&D biosystems	Cat# AF-261-NA RRID: AB_354430
P-EGFR(Y1068)	Cell Signaling Technology	Cat# 8543S RRID: AB_10828604
P-EGFR(Y1045)	Cell Signaling Technology	Cat #2237S RRID: AB_331710
P-EGFR(Y992)	Cell Signaling Technology	Cat #2235S RRID: AB_331708
P-EGFR(Y845)	Cell Signaling Technology	Cat #2231S RRID: AB_1264155
P-EGFR(Y1173)	Cell Signaling Technology	Cat #4407S RRID: AB_331795
EGFR	Cell Signaling Technology	Cat# 4267S RRID: AB_2246311
ERBB2	Cell Signaling Technology	Cat# 2165S RRID: AB_10692490
ERBB3	Cell Signaling Technology	Cat# 12708S RRID: AB_2721919
P-Akt(S473)	Cell Signaling Technology	Cat# 9271S RRID: AB_329825
Akt	Cell Signaling Technology	Cat# 9272S RRID: AB_329827
p-ERK(T202/Y204)	Cell Signaling Technology	Cat# 4376S RRID: AB_331772
ERK	Cell Signaling Technology	Cat# 4695S RRID: AB_390779
P-MEK(S217/221)	Cell Signaling Technology	Cat# 9121S RRID: AB_331648
MEK	Cell Signaling Technology	Cat# 9122S RRID: AB_823567
p-STAT5(Y694)	Cell Signaling Technology	Cat# 9351L RRID: AB_2315225
STAT5	Cell Signaling Technology	Cat# 9363S RRID: AB_2196923
V5-Tag (D3H8Q)	Cell Signaling Technology	Cat# 13202S RRID: AB_2687461
β-Actin (D6A8)	Cell Signaling Technology	Cat# 8457L RRID: AB_10950489
Cleaved Caspase 3	Cell Signaling Technology	Cat# 9664S RRID: AB_2070042
p-Tyr (PY20)	Santa Cruz Biotechnology	Cat# sc-508 RRID: AB_628122
p-Tyr (PY99)	Santa Cruz Biotechnology	Cat# sc-7020 RRID: AB_628123
Anti-Phosphotyrosine antibody	EMD millipore	Cat# 05-321 RRID: AB_309678
Vinculin Antibody	Cell Signaling Technology	Cat# 4650S RRID: AB_10559207
Bacterial and virus strains		
One Shot™ MAX Efficiency™ DH5α-T1^R Competent Cells	Thermos fisher scientific	Cat# 12297016
One Shot™ Stbl3™ Chemically Competent *E. coli*	Thermos fisher scientific	Cat# C737303
Biological samples		
Lung adenocarcinoma (grade III) with adjacent normal lung tissue microarray	US Biomax, Inc.	Cat# BS04081a
Lung carcinoma,92 cases, tumor and matched NAT*	US Biomax, Inc.	Cat# HLugA180Su03
Lung adenocarcinoma Tissue array with known EGFR and KRAS mutation status	Yale tissue microarrays (YTMA)	Cat# YTMA310
Chemicals, peptides, and recombinant proteins		
DMEM	Sigma-Aldrich	Cat# D5796
RPMI	Sigma-Aldrich	Cat# R8758

(*Continued on next page*)

Continued

REAGENT or RESOURCE	SOURCE	IDENTIFIER
SABM™ Small Airway Epithelial Cell Growth Basal Medium	LONZA	Cat# CC-3119
SingleQuots™ Supplements and Growth Factors	LONZA	Cat# CC-4124
Fetal Bovine Serum	GIBCO	Cat# 10437-028
Trypsin-EDTA	GIBCO	Cat# 25200-056
Penicillin-Streptomycin	GIBCO	Cat# 15140-122
Effectene Transfection Reagent	QIAGEN	Cat# 301427
Agarose, Low gelling	Sigma-Aldrich	Cat# A9045
Ultra-Low Attachment Multiple Well Plate	Sigma-Aldrich	Cat# CLS3473-24EA
Erlotinb (10nM,100nM,1μM)	Selleckchem	Cat# S1023
Trematinib(250 nM)	Selleckchem	Cat# S2673
Pictilisib(100 nM)	Selleckchem	Cat# S1065
Ruxolitinib(1 μM)	Cayman Chemicals	Cat# 11609
Critical commercial assays		
Proteome Profiler Mouse Phospho-RTK Array Kit	R&D biosystems	Cat# ARY014
Proteome Profiler Human Phospho-RTK Array Kit	R&D biosystems	Cat# ARY001B
Annexin V staining kit	BD Pharmingen	Cat #559763
Deposited data		
RNA-seq data	This paper	GSE101399
Experimental models: Cell lines		
HEK-293T	ATCC	ATCC CRL-3216
PC9	Sigma-Aldrich	90071810-1VL
NIH3T3	ATCC	ATCC CRL-1658
HCC2935	ATCC	ATCC CRL-2869
NCI-H460	ATCC	ATCC HTB-177
NCI-H358	ATCC	ATCC CRL-5807
NCI-H1437	ATCC	ATCC CRL-5872
HSAEC1-KT	ATCC	ATCC CRL-4050
Experimental models: Organisms/strains		
Mouse: NU/J homozygous (Male)	Jackson Laboratory	Stock No. 002019
Mouse: NSG (Male)	Jackson Laboratory	Stock No. 005557
Oligonucleotides		
	Forward Primer	Reverse Primer
Human ACPP	GGGCAAGAGAGCGAGACCCT	CCTCCTGCCTCAGCCTTCCA
Human ARHGAP6	ATGAGGTTCCCCTGGGTCGC	TGTCGGGTGGGGACTGGAAC
Human BTC	GGGTGCCAGCCTGGGAAGTA	CGGTCCATCAACCCCGCTCT
Human CALR3	GCCTGGAGCTTTGGCAGGTG	TTCCTCGCGGGCCTTCTTCA
Human CEACAM1	CGTGCTCGAAGCGTTCCTGG	TGGGCGGGTTCCAGAAGGTT
Human CYTIP	TCCAGCAGGGGTGCCTTCAG	GGGCAGGGTCCCAAACATGC
Human EVI2A	ACCAACACAATTCAGCGACAC	GTTGTAGGCAAGTGGTTGTCC
Human GAP43	GGCCGCAACCAAAATTCAGG	CGGCAGTAGTGGTGCCTTC
Human GPR149	GCAGTGGCCAAACGAGGTCC	TGGCTCCCCACACCTCTGTG

(*Continued on next page*)

Continued

REAGENT or RESOURCE	SOURCE	IDENTIFIER
Human ITGA2	CCTACAATGTTGGTCTCCCAA	AGTAACCAGTTGCCTTTTGGATT
Human MACC1	CCGAGGCGGGCAGATCACTA	TCCCGGGTTCACGCCATTCT
Human SEMA6D	GCTTTGTGCCTACATACTGCT	ACCGGATATTGCCTTGAATAGTG
Human SEMA7A	ACGGTTGCCTCATGTCCCGA	CGAGAGTTTGGGGCCAGGGA
Human ACTINB	GTCTTCCCCTCCATCGTGGG	CCTCTCTTGCTCTGGGCCTC
Mouse Acpp	ACCGTGAGTGGCCTGCAGAT	CAGCGTGAGTGGGTAGGGCT
Mouse Arhgap6	CACAACCTCTGCCCAGCTGC	TCCTGCTCGCTGGCTGAGAG
Mouse Btc	CTGCTCCTGGTCCTTGCCCT	GGGCACCGAGAGAAGTGGGT
Mouse Calr4	AGGCAAGAGGACGTCTGGGG	GCCACACCCAGTGTCTGTGC
Mouse Ceacam1	AAACCCAGCACCAGCCTCCA	TGGGGTGCTGCAGAAGGTGT
Mouse Cytip	TGGAAATCTGCTGGGGCCGA	TGAAGGCACCCCGGATGGAG
Mouse Evi2a	TGGGCCTCGTCGTCTTCTGG	GGCTTCTTGTGACCCACGGC
Mouse Gap43	TCGAGGAAAAGGCCGGCTCA	GGTGGTGGCAGCAGCATCAG
Mouse Gpr149	TGCTCCAGCCCATACGTGCT	AGAGCACTCTTCCCGCAGCA
Mouse Itga2	CTGGGAGCCCTGGATCGAGG	TTTCGCTCCTGGGAGGCCAA
Mouse Macc1	TGGAAGCCTCGAAACGCTCA	AGCTGCGTGATGTCCTCCAGA
Mouse Sema6d	CCCTGCTGTTGCGAGGAAGC	ACCTCCCTTCGTTTCCGGCA
Mouse Sema7A	GCTGGGGCTCCCTGGGATAG	TCCCCTGTCTCCCTCACCCA
Mouse ActinB	TCCTGACCGAGCGTGGCTAC	GGGAGGAAGAGGATGCGGCA
Human EGFR sgRNA#1	CACCGGTCTGCGTACTTCCAGACCA	AAACTGGTCTGGAAGTACGCAGACC
Human EGFR sgRNA#2	CACCGGTGGAGCCTCTTACACCCAG	AAACCTGGGTGTAAGAGGCTCCACC
Non-specific sgRNA	CACCGAAAAAGCTTCCGCCTGATGG	AAACCCATCAGGCGGAAGCTTTTTC
Recombinant DNA		
Plasmid: pLX304-BTC	Horizon Discovery	Cat# OHS1770-202320873
pBABE-Puro	Addgene	Clone ID. 21836
pBABE-EGFR-WT	Addgene	Clone ID. 11011
pBABE-EGFR-L858R	Addgene	Clone ID. 11012
pBABE-EGFR-L861Q	Addgene	Clone ID. 32068
pBABE-EGFR-Del1	Addgene	Clone ID. 32062
pLXSN-EGFR-WT	Addgene	Clone ID. 65226
pBABE-Hygro	Addgene	Clone ID. 1765
pBABE-Puro MEK-DD	Addgene	Clone ID. 15268
pLenti-CRISPR-V2	Addgene	Clone ID. 52961
BTC shRNA#1	UMASS Human pGIPZ library	Clone ID. V2LHS_150110
BTC shRNA#2	UMASS Human pGIPZ library	Clone ID. V2LHS_150114
Software and algorithms		
Prism 8.0	GraphPad	www.graphpad.com/scientificsoftware/prism
ImageJ	https://imagej.nih.gov/ij	N/A
Other		
Recombinant Human BTC Protein	R&D biosystems	Cat# 261-CE-010
Recombinant Human EGF Protein	R&D biosystems	Cat# 236-EG-200

RESOURCE AVAILABILITY

Lead contact

Further information about the protocols and requests for resources and reagents should be directed to and will be fulfilled by the lead contact, Narendra Wajapeyee (nwajapey@uab.edu).

Materials availability

All the materials and reagents described in this papers are available upon request from the lead contact.

Data and code availability

RNA-sequencing data presented in this paper are submitted to Gene Expression Ominibus (Accession No. GSE101399) and available publicly without restrictions. This paper does not report original code. Any additional information required to reanalyze the data reported in this paper is available from the lead contact upon request.

EXPERIMENTAL MODEL AND SUBJECT DETAILS

Cell culture

NIH3T3 and HEK-293T cells were purchased from the American Type Culture Collection (ATCC) and grown as recommended in Dulbecco's Modified Eagle Medium (DMEM) containing 10% FBS at 37°C in 5% CO_2. HCC2935, NCI-H460, NCI-H358, and NCI-H1437 cells were purchased from the American Type Culture Collection and grown as recommended in RPMI containing 10% FBS at 37°C in 5% CO_2, and PC9 cells were purchased From Sigma-Aldrich and grown as recommended in RPMI 10% FBS at 37°C in 5% CO_2. HSAEC1-KT cells were purchased from the ATCC and grown as recommended in SABM small airway epithelial cell-specific growth basal medium (Lonza Cat. No. CC-3119) along with singleQuots supplements and growth factors (Lonza Cat. No. CC-4124 (also see Key resources table).

Mouse tumorigenesis experiments

All protocols involving mice were approved by the Institutional Animal Care and Use Committee of the Yale University and University of Alabama at Birmingham. NIH3T3 cells (10 million cells) stably expressing empty vector or *BTC* were injected subcutaneously into five 5–6-week-old nude male mice per experimental group (Jackson Laboratory, Stock No. 002019, Bar Harbor, ME, USA). The tumor volume was then measured every week and calculated using the following formula: length × width^2 × 0.5. At the experimental endpoint, the tumors were measured, mice were sacrificed, and the tumors were isolated and imaged.

PC9 and HCC2935 cells (5 million cells) stably expressing non-specific shRNA, *BTC*-specific shRNA, *ERBB2*-specific shRNA, or *ERBB3*-specific shRNA were injected subcutaneously with Matrigel into five 5–6-week-old immunodeficient male NSG mice, per experimental group (Jackson Laboratory, Stock No. 005557). The tumor volume was then measured every week and calculated as described above. At the experimental endpoint, the tumors were measured, mice were sacrificed, and the tumors were isolated and imaged.

METHOD DETAILS

Plasmids and preparation of the lentiviral and retroviral stable cell lines

The lentiviral empty vector (pLX304) and *BTC* overexpression plasmids were purchased from Dharmacon (Clone ID. 6192). The retroviral-based expression vectors EGFR-WT, EGFR-L858R, EGFR-L861Q, and EGFR-DEL1(ΔE746-A750) were obtained from Addgene (Clone ID. 21836, 11011, 11012, 32068, 32062, respectively (key resources table). Gene-specific lentiviral shRNAs were obtained from Open Biosystems. The catalog numbers for the shRNAs are provided in Key resources table. Gene-specific lentiviral sgRNAs were cloned into the pLenti-CRISPR-V2 vector (Clone ID. 52961) obtained from Addgene; the sgRNAs sequences are provided in Key resources table. For lentivirus production, plasmids were transfected into HEK-293T cells along with the PDM2.G and psPAX2 packaging plasmids. For retrovirus production, pCMV-Gag-Pol and pCMV-VSV-G packaging plasmids were transfected using Effectene Transfection Reagent (Qiagen) per the manufacturer's instructions. After 48 hrs, the lentivirus/retrovirus-containing supernatants were harvested, filtered, and used for infections. Lentiviral shRNA-infected PC9 cells were selected using 0.6 μg/mL puromycin. Retrovirus-infected NIH3T3 cells were selected using 0.5 μg/mL puromycin.

RNA preparation, cDNA synthesis, and RT-qPCR analysis

Total RNA was extracted using TRIzol (Invitrogen) and purified using RNeasy Mini Columns (Qiagen) according to the manufacturer's instructions. We generated cDNA using the ProtoScript first strand cDNA synthesis kit (New England Biolabs) and then performed qPCR using the Power SYBR Green (Master Mix) (Life Technologies). The primer sequences are listed in Key resources table.

Immunoblotting

Immunoblot analysis was performed as described previously (Santra et al., 2009). Briefly, protein extracts were prepared in Pierce RIPA lysis buffer (Cat. No. 89901) supplemented with protease inhibitors (Roche) and phosphatase inhibitors (Sigma-Aldrich). Protein concentrations were estimated using the Pierce BCA Protein Assay according to the manufacturer's instructions. Protein extracts were separated using sodium dodecyl sulfate polyacrylamide gel electrophoresis (SDS-PAGE) and transferred onto a polyvinylidene difluoride (PVDF) membrane. Membranes were incubated with the primary antibodies listed in Key resources table and appropriate secondary antibodies. SuperSignal West Pico (Pierce) or Femto Reagent (Pierce) was used for detecting the proteins.

MTT assays

For MTT assays, 3×10^3 NIH3T3 cells were plated in triplicate in a volume of 100 μL in 96-well plates. After 24 hrs, the EGFR inhibitor erlotinib was administered at defined concentrations, as indicated in the figures and figure legends. Cell viability was evaluated after 5 days of treatment. To this end, 20 μL of 5 mg/mL MTT solution dissolved in 1× PBS was added to each well of the 96-well plate and incubated for 1hrat 37°C. The MTT solution was then gently removed, and 100 μL DMSO was added to each well. After mixing well by pipetting, the absorbance was measured at 590 and 630 nm using a Biotek Synergy MX MultiFormat Microplate Reader. The average measurement at 630 nm was subtracted from the average at 590 nm, and the relative growth rate was plotted with respect to vehicle control-treated cells.

Soft agar assay

We used soft agar assays to analyze anchorage-independent growth. Briefly, we seeded 2×10^4 NIH3T3 cells stably expressing either an empty vector control or a *BTC* expression vector for overexpression experiments or 5×10^3 PC9 lung cancer cells expressing either a non-silencing shRNA control or a BTC shRNA for knockdown experiments. Cells were embedded into 0.4% low-melting agarose (Sigma-Aldrich) and layered on top of a 0.8% agarose base. After 2 weeks of growth, the cells were fixed and stained with crystal violet.

RNA-seq and data analysis

NIH3T3 cells stably expressing empty vector, EGFR-WT, EGFR-L858R, EGFR-L861Q, and EGFR-Del(E746-A750) were used to prepare total RNA, which was then used for gene expression analysis on an Illumina HiSeq 2500 system in biological triplicates. Total RNA was extracted using Trizol reagent (Invitrogen) according to the manufacturer's instructions and then purified on RNAeasy Mini Columns (Qiagen) according to the manufacturer's instructions. mRNA was purified from approximately 500 ng total RNA using oligo-dT beads and then sheared by incubation at 94°C. Following first-strand synthesis with random primers, second-strand synthesis was performed with dUTP to generate strand-specific sequencing libraries. The cDNA library was then end-repaired and A-tailed. Adapters were then ligated, and second-strand digestion was performed using uracil-DNA-glycosylase. Indexed libraries that met appropriate cut-offs for both were quantified by qRT-PCR using a commercially available kit (KAPA Biosystems). The insert size distribution was determined using LabChip GX or an Agilent Bioanalyzer. Samples with a yield $\geq$ 0.5 ng/μl were used for sequencing on the Illumina HiSeq 2500 system. Images generated by the sequencers were converted into nucleotide sequences by the base-calling pipeline RTA 1.18.64.0 and stored in FASTQ format. The raw sequencing data in the FASTQ files were subjected to a quality check (FastQC), removal of adapter content, and quality thresholding (removal of reads with Phred score < 30). Reads that passed the quality thresholds were mapped to the latest stable version of the Mouse reference genome mm10 (GRCm38/mm10, Ensembl) using Bowtie2 and Tophat 2.1.1. The expression of the assembled transcriptomes was estimated using Cufflinks 2.2.1 (Trapnell et al., 2012). Briefly, the quality of the assemblies was assessed, and the normalized gene and transcript expression profiles were computed for each sample. The normalization was performed using the classic fragments per kilobases per million fragments (FPKM) method followed by Log2 transformation. The gene-level differential expression between conditions was estimated using the Log2-transformed FPKM values of transcripts sharing each gene ID. The uncorrected p-value of the test statistic and the false discovery rate (FDR)-adjusted p-value of the test statistic (q-value) were estimated for differentially expressed genes (DEGs). Any gene with a p-value greater than the FDR after Benjamini-Hochberg correction for multiple testing was deemed to be differentially expressed between the test condition and control condition. The RNA-seq data have been submitted to GEO (Accession No. GSE101399).

Immunohistochemistry

Formalin-fixed, paraffin-embedded tissue microarray (TMA) slides containing LUAD and matched normal lung tissues were obtained from US Biomax, Inc. (Cat. Nos. BS04081a, HLugA180Su03) and YTMA310 from Yale University. Briefly, following deparaffinization of the slides, antigen retrieval was performed in citrate buffer (pH 6.0) at 97°C for 20 min using the Lab Vision PT Module (Thermo Scientific). Endogenous peroxides were blocked using hydrogen peroxide for 30 min. The slides were then washed with 1 × Tris-buffered saline (TBS), and proteins were blocked using 0.3% bovine serum albumin (BSA) for 30 min. Slides were incubated in BTC antibody (dilution 1:125), followed by incubation with secondary anti-mouse HRP-conjugated antibody (Dako). Slides were then stained using the Dako Liquid DAB+ Substrate Chromogen System and counterstained with Dako Automation Hematoxylin Histological Staining Reagent (Thermo Scientific). The intensity of cytoplasmic expression of BTC was scored as negative 0, weak 1+, moderate 2+ and strong 3+ following the scoring approach described in previously published studies (Khelwatty et al., 2017; Sun et al., 2009). BTC staining was scored by Dr. Xuchen Zhang, who was blinded regarding the identity of the samples. All antibodies used for immunohistochemistry analyses are listed in Key resources table.

Mouse RTK arrays

The Proteome Profiler Mouse Phospho-RTK Array Kit (R&D Systems) was used measure the relative levels of tyrosine phosphorylation for 39 distinct RTKs according to the manufacturer's protocol. Briefly, cell lysates were prepared from vector- and *BTC*-expressing NIH3T3 cells using RIPA lysis buffer (Invitrogen) containing protease and phosphatase inhibitors [Protease Inhibitor Cocktail (Roche) and Phosphatase Inhibitor Cocktail (Sigma-Aldrich)]. After blocking for 1 hr with Array Buffer 1 (R&D Systems), the arrays were incubated with 200 μg protein lysate overnight at 4°C. Arrays were then washed in Wash Buffer (R&D Systems) and incubated with a horseradish peroxidase-conjugated phospho-tyrosine detection antibody (1:5000) for 1 hr. Finally, arrays were developed using the SuperSignal West Pico Reagent (Pierce) to detect changes in phosphorylation. Signal intensities were quantified using ImageJ software. Positive controls on the membranes were used to normalize the results and compare the results from different membranes.

Human RTK arrays

The Proteome Profiler Human Phospho-RTK Array Kit (R&D Systems) was used determine the relative levels of tyrosine phosphorylation for 49 distinct RTKs, according to the manufacturer's protocol. Briefly, cell lysates were prepared from PC9 cells expressing either *BTC* or non-silencing (NS) control shRNAs using RIPA lysis buffer (Invitrogen) containing protease and phosphatase inhibitors [Protease Inhibitor Cocktail (Roche) and Phosphatase Inhibitor Cocktail (Sigma-Aldrich)]. After blocking for 1 h with Array Buffer 1 (R&D Systems), the arrays were incubated with 200 μg protein lysate, overnight at 4°C. Arrays were washed in Wash Buffer (R&D Systems), and incubated with a horseradish peroxidase-conjugated phospho-tyrosine detection antibody (1:5000) for 1 h. Finally, arrays were developed using the SuperSignal West Pico Reagent (Pierce) to detect changes in phosphorylation. Signal intensities were quantified using Image J software. Positive controls on the membranes were used to normalize the results and compare the results from different membranes.

Immunoprecipitation

Whole cell lysates (1 mg) were incubated with a cocktail of phosphotyrosine antibodies (pY20, sc-508, sc-7020, pY99, Santa Cruz Biotechnology; 4G10, 05-321, EMD Millipore) and rotated end-over-end at 4°C overnight. Protein A/G agarose beads (Invitrogen) were washed with lysis buffer, added to the lysates, and rotated end-over-end at 4°C for 2 hrs. Beads were collected by centrifugation, and a sample of the supernatant was kept as a pass-through. The beads were washed 3 × with lysis buffer, and proteins were eluted by heating the samples to 100°C for 5 minutes in 2 × SDS sample buffer. The immunoprecipitated proteins were separated by SDS-PAGE, transferred to PVDF membranes, and probed with the EGFR, ERBB2, and ERBB3 antibodies (Cell Signaling Technology).

Cell viability assay in ultra-low attachment plates

Cells were seeded onto Corning Ultra-Low Attachment Surface (Cat. No. CLS3473) in 24-well plates at 50,000 cells/well in triplicate and incubated for the indicated days. After incubation, cells were collected and mixed with 0.4% typhon blue solution. To calculate cell viability, both live and dead cell counts were recorded for each set, and the percentage of cell viability was calculated using the formula: Total live cells/Total cells × 100.

Annexin V assay

Apoptosis rates were analyzed using an Annexin V staining kit (BD Pharmingen #559763) per manufacturer's protocol. Briefly, 5000 cells/well were plated in an ultra-low attachment 96-well plate. After 5 days, cells were collected, washed twice with 1× PBS, resuspended in 1× binding buffer, stained with 5μlPE Annexin V, and incubated for 15 min in the dark. After incubation, 400 μl of 1× binding buffer was added, and images were captured using a florescent microscope (10× magnification).

QUANTIFICATION AND STATISTICAL ANALYSIS

All experiments were conducted in at least three biological replicates. Results for individual experiments are expressed as the mean ± SEM. For measurement of tumor progression in mice and MTT assays, statistical analyses were performed by analyzing the area under the curve using Prism version 7.0 for Macintosh (GraphPad Software; https://www.graphpad.com). For the remaining experiments, *P* values were calculated using the two-tailed unpaired Student's *t* test in Prism.